

Low-dimensional model of the large-scale circulation of turbulent Rayleigh-Bénard convection in a cubic container

Dandan Ji

Department of Physics, Yale University, New Haven, Connecticut 06511, USA

Eric Brown ^{*}

*Department of Mechanical Engineering and Materials Science, Yale University,
New Haven, Connecticut 06511, USA*



(Received 25 December 2019; accepted 20 May 2020; published 12 June 2020)

We test the ability of a low-dimensional turbulence model to predict how dynamics of large-scale coherent structures such as convection rolls change in different cell geometries. The model consists of stochastic ordinary differential equations, which were derived from approximate solutions of the Navier-Stokes equations. We test the model using Rayleigh-Bénard convection experiments in a cubic container, in which there is a single convection roll known as the large-scale circulation (LSC). The model describes the motion of the orientation θ_0 of the LSC as diffusion in a potential determined by the shape of the cell. The model predicts advected oscillation modes, driven by a restoring force created by the noncircular shape of the cell cross section. We observe the corresponding lowest-wave-number predicted advected oscillation mode in a cubic cell, in which the LSC orientation θ_0 oscillates around a corner, and a slosh angle α rocks back and forth, which is distinct from the higher-wave-number advected twisting and sloshing oscillations found in circular cylindrical cells. Using the Fokker-Planck equation to relate probability distributions of θ_0 to the potential, we find that the potential has quadratic minima near each corner with the same curvature in both the LSC orientation θ_0 and slosh angle α , as predicted. To quantitatively test the model, we report values of diffusivities and damping timescales for both the LSC orientation θ_0 and temperature amplitude for the Rayleigh number range $8 \times 10^7 \leq \text{Ra} \leq 3 \times 10^9$. The new oscillation mode around corners is found above a critical $\text{Ra} = 4 \times 10^8$. This critical Ra appears in the model as a crossing of an underdamped-overdamped transition. The natural frequency of the potential, oscillation period, power spectrum, and critical Ra for oscillations are consistent with the model if we adjust the model parameters by up to a factor of 2.9, and values are all within a factor of 3 of model predictions. However, these uncertainties in model parameters are too large to correctly predict whether the system is in the underdamped or overdamped state at a given Ra. Since the model was developed for circular cross sections, the success of the model at predicting the potential and its relation to other flow properties for a square cross section—which has different flow modes than the circular cross section—suggests that such a modeling approach could be applied more generally to different cell geometries that support a single convection roll.

DOI: [10.1103/PhysRevFluids.5.064606](https://doi.org/10.1103/PhysRevFluids.5.064606)

*ericmichealbrow@gmail.com

I. INTRODUCTION

While turbulent flows are often thought of as irregular and erratic, large-scale coherent flow structures are commonplace in turbulence. Examples of such structures include convection rolls in the atmosphere, oceans, and many other geophysical flows. Such structures and their dynamics can play a significant role in heat and mass transport.

A particular challenge is to predict the dynamical states of these large-scale flow structures, and how they change with different boundary geometries, for example in the way that local weather patterns depend on the topography of the Earth's surface. The Navier-Stokes equations that describe flows are impractical to solve for such turbulent flows, so low-dimensional models are desired. It has long been recognized that the dynamical states of large-scale coherent structures are similar to those of low-dimensional dynamical systems models [1] and stochastic ordinary differential equations [2–5]. However, such models tend to be descriptive rather than predictive, as parameters are typically fit to each observation, rather than derived from fundamentals such as the Navier-Stokes equations [6]. In particular, such dynamical systems models tend to fail at quantitative predictions of new dynamical states in regimes outside where they were parameterized. Our goal is to develop and test a general low-dimensional model that can quantitatively predict the different dynamical states of large-scale coherent structures in different geometries.

We test the application of a low-dimensional model to different geometries in the model system of turbulent Rayleigh-Bénard convection. In Rayleigh-Bénard convection, a fluid is heated from below and cooled from above to generate buoyancy-driven flow [7,8]. This system exhibits robust large-scale coherent structures that retain a similar organized flow structure over a long time. For example, in containers of aspect ratio near 1, a large-scale circulation (LSC) forms. This LSC consists of localized blobs of coherent fluid known as plumes. The plumes collectively form a single convection roll in a vertical plane that can be identified with appropriate averaging over the flow field or timescales on the order of a turnover period of the circulation [9]. This LSC spontaneously breaks the symmetry of symmetric containers, but turbulent fluctuations cause the LSC orientation θ_0 in the horizontal plane to meander spontaneously and erratically and allow it to sample all orientations [10]. While the LSC exists nearly all of the time, on rare occasions these fluctuations lead to spontaneous cessation followed by reformation of the LSC [10,11]. In circular cross-section containers, the LSC exhibits an oscillation mode [12–24] consisting of twisting and sloshing [25–28], and in some cases a jump-rope-like oscillation [29]. The Coriolis force causes a rotation of the LSC orientation [30–32].

There are several low-dimensional models for various aspects of LSC dynamics [33–41]. Of these, only a few attempt to address geometry dependence of dynamics. In one, an approximate analytical model was applied to ellipsoidal containers, which predicted an oscillation with a geometry-dependent restoring force [36]. However, the methods used could not be applied to other geometries. Brown and Ahlers proposed a model of diffusive motion in a potential well, which is formulated in a way that it can make predictions for a wide variety of container geometries based on predictions of the potential as a function of the container cross-section geometry [2,37,42].

The model of Brown and Ahlers and its extensions have successfully described most of the known dynamical modes of the LSC in circular horizontal cross-section containers including the meandering, cessations, and oscillation modes described above [28,31,32,37,42], with the exception of the recently observed jump rope mode which has not yet been modeled. The combination of twisting and sloshing oscillation modes [25–28] can alternatively be described in this model as a single advected oscillation mode with two oscillation periods per LSC turnover period [28]. Predictions are typically quantitatively accurate within a factor of 2, but can be more accurate when more fit parameters are used [43].

While a circular cross section is the trivial case of that model when it comes to geometry dependence (i.e., the geometry-dependent term was equal to zero), the model of Brown and Ahlers has also successfully described some states and dynamics that are unique to noncircular cross-section containers. In a container with rectangular horizontal cross section, the model

describes the preferred alignment of the LSC orientation θ_0 with the longest diagonals, and an oscillation of θ_0 between nearest-neighbor diagonals [44]. The model also successfully predicted the existence of a stochastic switching of the LSC orientation between adjacent corners of a cubic container [40,41,45–48], including a quantitative prediction of the frequency of events, and how it varies with the flow strength [46].

In this paper, we test a couple of geometry-dependent predictions of the model that to our best knowledge have not yet been tested quantitatively. One of these predictions is how the probability distribution of the LSC orientation is affected by the container geometry, which directly connects to the potential that provides a forcing to the LSC orientation via the Fokker-Planck equation. In a cubic cell, for example, the geometry is predicted to lead to four preferred orientations aligned with the diagonals of the cell [42]. While it has been known since before the development of the model the LSC tends to align with the diagonals of a cubic container [49–52], the probability distribution has not yet been quantitatively compared to the prediction, and thus the potential has not been characterized. The second quantitatively untested prediction of the model relates to the advected oscillation mode of the LSC around corners of a cell [42,44]. While oscillations around the longest diagonals of a cross section have now been observed in horizontal cylinders [44] and a cube [40], quantitative tests of the model have not yet been reported regarding the frequency and power spectrum. This test includes a prediction of a different structure of the advected oscillation mode in noncircular cross sections which has not yet been observed: an oscillation in θ_0 in phase at all heights and sloshing oscillation out of phase in the top and bottom halves of the cell [28].

The remainder of this paper is organized as follows. The low-dimensional model of Brown and Ahlers is summarized in Sec. II. Details of the experimental apparatus design, calibrations, and methods used to characterize the LSC orientation are described in Sec. III. Probability distributions to characterize the model potential and compare to predictions are presented in Sec. IV. The detailed prediction for the advected oscillation and measured power spectra are presented in Sec. V. Predictions of the oscillation structure and the correlation functions used to characterize it are presented in Sec. VI. The frequency of measured oscillations for different Rayleigh numbers to test the conditions for the existence of the oscillations is presented in Sec. VII. Measurements of the different model parameters to apply the model to cubic containers and make comparisons to predictions and measurements in other geometries are presented in Appendix A.

II. REVIEW OF THE LOW-DIMENSIONAL MODEL

In this section we summarize the model of Brown and Ahlers, including its geometry-dependent potential [37]. The model consists of a pair of stochastic ordinary differential equations, using the empirically known, robust LSC structure as an approximate solution to the Navier-Stokes equations to obtain equations of motion for parameters that describe the LSC dynamics. The effects of fast, small-scale turbulent fluctuations are separated from the slower, large-scale motion when obtaining this approximate solution, then added back in as a stochastic term in the low-dimensional model. The flow strength in the direction of the LSC is characterized by the temperature amplitude δ , corresponding to half the temperature difference from the the upward-flowing side of the LSC to the downward-flowing side. The equation of motion for δ is

$$\dot{\delta} = \frac{\delta}{\tau_\delta} - \frac{\delta^{3/2}}{\tau_\delta \sqrt{\delta_0}} + f_\delta(t). \quad (1)$$

The first forcing term on the right side of the equation corresponds to buoyancy, which strengthens the LSC, followed by damping, which weakens the LSC. δ_0 is the stable fixed point value of δ where buoyancy and damping balance each other, and τ_δ is a damping timescale for changes in the strength of the LSC. $f_\delta(t)$ is a stochastic forcing term representing the effect of small-scale turbulent fluctuations and is modeled as Gaussian white noise with diffusivity D_δ .

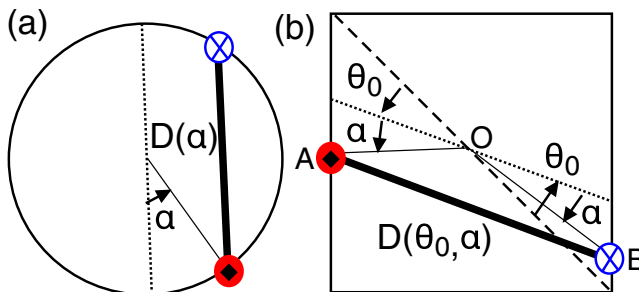


FIG. 1. (a) Top view of a circular cross-section container. (b) Top view of a square cross-section container. In each case, the circulation plane of the LSC is indicated by the thick solid line, and the hot side is indicated by the circle with a diamond in the center, while the cold side is indicated by the circle with a cross in the center. The slush angle α is defined by the lateral displacement of the plane of circulation away from a line going through the cell center (dotted line). The orientation of the LSC is defined as the angle θ_0 of the hot side of the center line (dotted line) relative to a corner in a cube (dashed line). The length of the circulation plane $D(\theta_0, \alpha)$ across a horizontal cross section determines the model potential in Eq. (3).

The equation of motion for the LSC orientation θ_0 is

$$\ddot{\theta}_0 = -\frac{\dot{\theta}_0 \delta}{\tau_{\dot{\theta}} \delta_0} - \nabla V_g(\theta_0, \alpha) + f_{\dot{\theta}}(t). \quad (2)$$

The first term on the right side of the equation is a damping term where $\tau_{\dot{\theta}}$ is a damping timescale for changes of orientation of the LSC. $f_{\dot{\theta}}$ is another stochastic forcing term with diffusivity $D_{\dot{\theta}}$. V_g is a potential which physically represents the pressure of the sidewalls acting on the LSC. Equation (2) is mathematically equivalent to diffusion in a potential landscape $V_g(\theta_0, \alpha)$.

The potential is given by

$$V_g(\theta_0, \alpha) = \left\langle \frac{3\omega_{\phi}^2 H^2}{4D(\theta_0, \alpha)^2} \right\rangle_{\gamma}, \quad (3)$$

where ω_{ϕ} is the angular turnover frequency of the LSC, and H is the height of the container [42]. $D(\theta_0, \alpha)$ is the distance across a horizontal cross section of the cell, as a function of θ_0 and α as shown in Fig. 1. The notation $\langle \dots \rangle_{\gamma}$ represents a smoothing of the potential over a range of $\gamma = \pi/10$ in θ_0 due to the nonzero width of the LSC [44]. Equation (3) includes an update to the numerical coefficient, given here for aspect ratio 1 containers [44]. This expression assumes a mean solution for $\delta = \delta_0$ as an approximation to ignore any δ dependence in the potential. The diameter function $D(\theta_0, \alpha)$ can be evaluated for any cross-sectional geometry, with the caveat that in this form of the model the geometry must support a single-roll LSC. In practice, this requires aspect ratios of order 1 and assumes the horizontal cross-section variation affects the flow structure more than any variation with height. Since $D(\theta_0, \alpha)$ can be calculated for a given geometry as illustrated in Fig. 1, then $V_g(\theta_0, \alpha)$ can be predicted explicitly (for example, shown in Fig. 2 for a square cross section [42,46]). Equation (2) can then be solved statistically for any cross section that has a single-roll LSC. Predictions exist for δ_0 , $\tau_{\dot{\theta}}$, and τ_{δ} using approximation solutions of the Navier-Stokes equations [37]. The only parameters that have not been predicted are the constants $D_{\dot{\theta}}$ and D_{δ} , which in principle could be predicted from models of turbulent kinetic energy in future work. In practice, $D_{\dot{\theta}}$ and D_{δ} , $\tau_{\dot{\theta}}$, and τ_{δ} can all be obtained from independent measurements of the mean-square displacement of $\dot{\theta}_0$ and δ over time, and δ_0 can be obtained from the peak of the probability distribution of δ [37]. Short-term measurements from sparse data can then be used as input to the model to make predictions of more complex dynamics such as oscillation structures and stochastic barrier crossing.

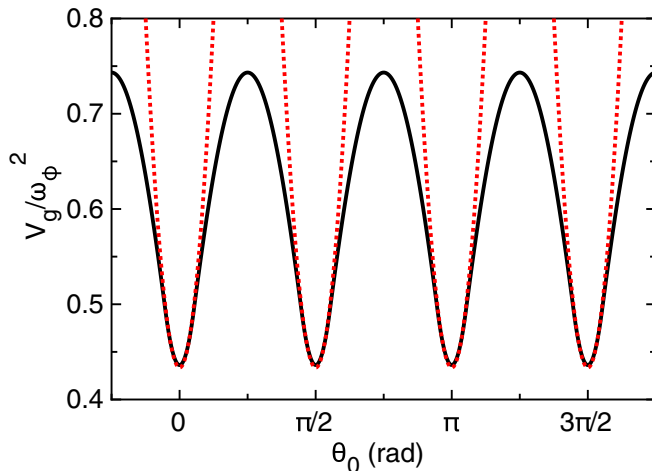


FIG. 2. The model potential $V_g(\theta_0)$ for a cubic cell when $\alpha = 0$, normalized by ω_ϕ^2 to make it purely a function of container geometry. Solid line: exact expression from Eq. (3). Dotted lines: quadratic approximations around each potential minimum. The potential minima correspond to the four corners of the cell. Equation (2) describes diffusive fluctuations of θ_0 in this potential, in which θ_0 can occasionally cross the barriers to switch between corners or oscillate around a potential minimum.

Equations (1) and (2) have mainly been applied to describe LSC dynamics in circular-cross-section containers. Most of the time, δ fluctuates around its stable fixed point at δ_0 in Eq. (1). Occasionally, cessations occur when δ drops to near zero. When these cessations occur, the damping term in Eq. (2) weakens, allowing larger diffusive meandering in θ_0 [37]. Additional forcing terms in Eqs. (1) and (2) due to tilting the cell relative to gravity produced a potential minimum in the plane of the tilt [42]. If a cell is tilted far enough, this can provide enough of a restoring force to overcome damping, and an oscillation can then be driven by turbulent fluctuations which provide a broad spectrum noise to drive oscillations at the resonant frequency of the potential [42]. Oscillations observed in leveled circular cross-section containers are a combination of twisting [25,53] and sloshing [26,27] oscillation modes. This combination can alternatively be described as a single advected oscillation mode based on an extension of Eq. (2) to include advection in the direction of the LSC motion [28]. The restoring force comes from the potential of Eq. (3) increasing as the diameter $D(\alpha)$ changes as the slosh angle α oscillates, as illustrated in Fig. 1(a). In this case, while there is still a turbulent background driving a broad spectrum of frequencies, advection in a closed loop limits the solutions with constructive interference to those that have integer multiples of the frequency of the LSC turnover, and only even-order modes have a restoring force in α for a circular cross section (corresponding to the twisting and sloshing modes).

The geometry-dependent potential $V_g(\theta_0, \alpha)$ can produce different LSC dynamics. For example, oscillations can occur around a potential minimum at a corner of a cell [40,44]. Large fluctuations can lead to the LSC crossing potential barriers between wells if the fluctuation energy level $D_\theta \tau_\theta$ is not too much smaller than the potential barrier height ΔV_g [46]. In rectangular cross-section cells, the potential barrier heights shrink along the shorter sides of the rectangle, leading to more frequent barrier crossings [44], and periodic oscillations between neighboring potential minima also occur if $D_\theta \tau_\theta$ is larger than ΔV_g [44]. A cubic cell was chosen to study oscillations around corners because it has the potential minima around corners to provide a restoring force for oscillations, while there are no lowered potential barriers between neighboring corners, which suppresses periodic oscillations between neighboring corners. Detailed predictions for the potential and oscillations in a cubic geometry are given in Secs. IV and VA and Appendix C.

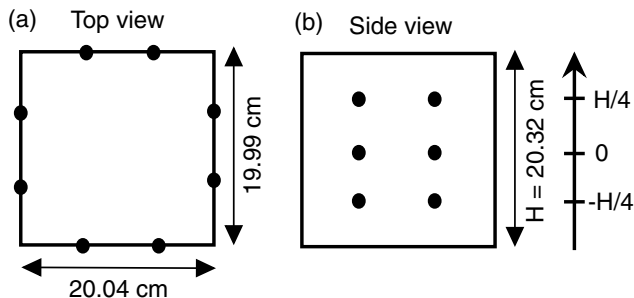


FIG. 3. A schematic of the experimental setup. (a) Top view. (b) Side view. Thermistor locations on the sidewall are indicated by circles.

III. THE EXPERIMENTAL APPARATUS AND METHODS

A. Apparatus

The design of the apparatus was based on an earlier circular cylindrical cell [54] but with a cubic flow chamber instead. It is the same apparatus used in Ref. [46], but described here for the first time in detail. The flow chamber is nearly cubic, with height $H = 20.32$ cm, and horizontal dimensions measured at the top and bottom plates of 20.04 cm and 19.99 cm, as is shown in Fig. 3.

To control the temperature difference ΔT between the top and bottom of the cell, water was circulated through top and bottom plates, each by a temperature-controlled water bath. The plates were aluminum, with double-spiral water-cooling channels as in Ref. [55], except that the inlet and outlet of each plate were adjacent to minimize the spatial temperature variation within the plates. Each plate had five thermistors to record control temperatures, with one at the center and one on the diagonal between the center and each corner of the plate. The top and bottom plate were parallel within 0.06° .

The sidewalls were plexiglas to thermally insulate the cell from the surroundings. Three out of four of the sidewalls had a thickness of 0.55 cm. The fourth sidewall (referred to as the middle wall) was shared with another identical flow chamber to be used in future experiments. The middle wall had a thickness of 0.90 cm to thermally insulate the chambers from each other.

The flow chamber was further insulated from the room as in Ref. [55] with 5 cm thick closed-cell foam around the cell, surrounded on the sides by a copper shield with water at temperature $23.00 \pm 0.02^\circ\text{C}$ circulating through a pipe welded to the shield. The shield was surrounded by an outer layer of 2.5 cm thick open-cell foam.

To measure the LSC, thermistors were mounted in the sidewalls as in Ref. [30]. There were three rows of thermistors at heights $-H/4$, 0 , and $H/4$ relative to the middle height, as shown in Fig. 3. In each row there were eight thermistors lined up vertically and equally spaced in the angle θ measured in a horizontal plane, as shown in Fig. 3(a).

On the three outer walls, the thermistors were mounted in blind holes drilled into the sidewall from outside, 0.05 cm away from the fluid surface. To mount the thermistors in the middle wall, two grooves were cut on each side of the middle wall in which to place the thermistors and run wiring through the grooves and out the holes in the top plate. The thickness of the width of the middle wall between the grooves was reduced to 0.27 cm. The remaining space in the grooves was filled with silicon sealant so the flow chambers remained thermally insulated from each other. The silicon sealant protruded out of the grooves by as much as 0.17 cm over a surface area $1.78 \text{ cm} \times 0.40 \text{ cm}$. Silicon sealant was also used to seal the four edges where the sidewalls meet along the height of the cell which stuck out less than 0.1 cm in a region within 0.5 cm of the edge along the wall. The sidewalls bowed out by up to 0.07 cm at the midheight near the middle wall. The top and bottom plate each had a small hole of diameter 0.17 cm, and the middle wall had a hole of diameter

0.2 cm in a corner, which was mostly above the level of the top plate, for filling, degassing, and pressure release of the flow chamber. All of the aforementioned variations away from a perfectly cubic cell can introduce asymmetries that in principle can affect the flow dynamics [30]. However, we will confirm in Sec. IV that the cubic shape is the dominant geometric factor, and that nonuniformities in the plate temperature are the largest source of asymmetry in measurements (Secs. III E and IV A 4).

The alignment of the LSC can also be controlled with a small tilt of the cell relative to gravity [9]. Unless otherwise specified, we report measurements with the cell tilted at an angle of $\beta = (1.0 \pm 0.2)^\circ$ relative to gravity, in the plane along a diagonal at orientation $\theta_\beta = 0 \pm 0.03$ rad, to lock the LSC orientation near one diagonal and suppress diagonal-switching.

The working fluid was degassed and deionized water with mean temperature of 23.0°C , for a Prandtl number $\text{Pr} = \nu/\kappa = 6.41$, where $\nu = 9.36 \times 10^{-7}$ m²/s is the kinematic viscosity and $\kappa = 1.46 \times 10^{-7}$ m²/s is the thermal diffusivity. The Rayleigh number is given by $\text{Ra} = g\alpha_T \Delta T H^3 / \kappa \nu$ where g is the acceleration of gravity, and $\alpha_T = 0.000238/\text{K}$ is the thermal expansion coefficient. Unless otherwise specified, we report measurements at $\Delta T = 18.35^\circ\text{C}$ for $\text{Ra} = 2.62 \times 10^9$.

B. Thermistor calibration

The thermistors in the top and bottom plates were calibrated together inside a water bath. The thermistors embedded in the sidewalls were calibrated inside the cell every few months relative to the plate temperatures. The calibrations identified systematic errors in temperature measurements of $T_{\text{err}} = 4$ mK, mostly due to drift in thermistor behavior between calibration checkpoints. Fluctuations of recorded temperature in equilibrium had a standard deviation of 0.7 mK, corresponding to the random error on temperature measurements. Deviations from the calibration fit function were typically 6 mK for the plate thermistors, which are much smaller than systematic effects of the top and bottom plate temperature nonuniformity (see Sec. III E).

C. Obtaining the LSC orientation θ_0

To characterize the LSC in a noisy background of turbulent fluctuations, we use the function

$$T = T_0 + \delta \cos(\theta - \theta_0) \quad (4)$$

to obtain the orientation θ_0 and strength δ of the LSC [10]. This is fit to measurements of the eight sidewall thermistor temperatures in the same row every 9.7 s. An example of the temperature profile measured by the sidewall thermistors for one time step at the middle row for $\text{Ra} = 2.62 \times 10^9$ is shown in Fig. 4 along with the cosine fit. Deviations from the cosine fit at one instant are mostly due to local temperature fluctuations from turbulence. Propagating the error on the thermistor measurements from Sec. III B leads to systematic uncertainties of $\Delta\theta_0 = T_{\text{err}}/\delta\sqrt{8} = 1.5/\delta$ mK/rad and $\Delta\delta = T_{\text{err}}/\sqrt{8} = 1.5$ mK, corresponding to 0.003 rad and 0.3% errors, respectively, at our typical $\text{Ra} = 2.62 \times 10^9$. Throughout this paper, we present data for the middle row thermistors only, unless otherwise stated.

D. Obtaining the slosh angle α

Some oscillations of the LSC shape can be characterized in terms of the slosh angle α [26–28]. We use the same definition of the slosh angle α as in Ref. [28] based on the shift in the extrema of the profile $T(\theta)$ away from θ_0 . The temperature profile is quantified by the Fourier series

$$T = T_0 + \delta \cos(\theta - \theta_0) + \sum_{n=2}^4 A_n \sin[n(\theta - \theta_0)] \quad (5)$$

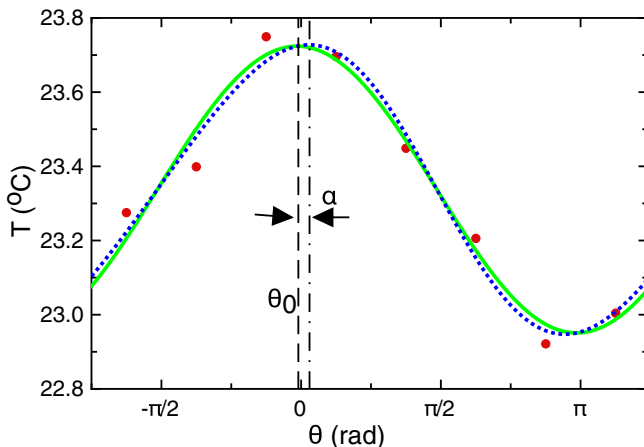


FIG. 4. Example of the temperature profile measured by the sidewall thermistors. Solid curve: cosine fitting which gives the LSC orientation θ_0 and amplitude δ . Dotted curve: fit of the cosine term plus the second-order sine term A_2 . The shift in peak locations (vertical lines) between the two curves defines the slosh angle α .

at each point in time, where the Fourier moments are

$$A_n = \frac{1}{4} \sum_{i=1}^8 [T_i - T_0 - \delta \cos(\theta - \theta_0)] \sin[n(\theta - \theta_0)]. \quad (6)$$

Here the sum over i corresponds to the sum over different thermistors. Moments are calculated only up to fourth order due to the Nyquist limit with eight temperature measurement locations. We do not include cosine terms since they are relatively small [56] and do not shift the extrema of the temperature profile much. A_1 is not included because it is trivially zero since we first fit to Eq. (4).

Following the procedure of Ref. [28], the slosh angle α is calculated as the shift of the positions of the extrema of the temperature profile from the sum of the δ term and A_2 term only in Eq. (5), which yields the implicit equation $\delta \sin \alpha = 2A_2 \cos(2\alpha)$ to solve for α . An example of this fitting is shown as the dotted line in Fig. 4. Note that A_2 is small compared to the variation around the fit due to turbulent fluctuations, so measurements of A_2 include significant noise, but we will see in Sec. VI that an oscillation structure can still be determined from a power spectrum of A_2 , as was found for cylindrical cells [28]. The absolute error on A_2 is the same as the error on δ , since both are the result of fitting the same temperature profile. Propagating the temperature measurement error of $\Delta T_{\text{err}} = 4.1$ mK results in the systematic error $\Delta \alpha \approx 2\Delta A_2/\delta = 0.007$ rad in the small α limit (since A_2 is much smaller than δ) at $\text{Ra} = 2.62 \times 10^9$. The ratio of errors on $\Delta \alpha/\Delta \theta_0 = 4\sqrt{2}\Delta A_2/\Delta T_{\text{err}} = 2.3$ indicates that α is more sensitive to temperature forcing than θ_0 .

E. Effects of the plate temperature nonuniformity

We quantify the variation of the top and bottom plate temperatures because it has been shown that even a slight variation in temperature profile can have a large affect on the alignment of the LSC [30]. The spatial variation of the temperature within each plate is shown in Fig. 5. These measurements were done in a level cell ($\beta = 0^\circ \pm 0.003^\circ$). We show the mean temperature of each thermistor T_i normalized as $\langle T_i - T_0 \rangle / \Delta T$, where T_0 is the average temperature of the five thermistors in the same plate. The standard deviation of $T_i - T_0$ is $0.005\Delta T$, which is more uniform than previous experiments [55]. It can be seen in Fig. 5 that the ratio for each thermistor is consistent for different ΔT , indicating this is a systematic effect coming from imperfections in the plates and cooling channel design.

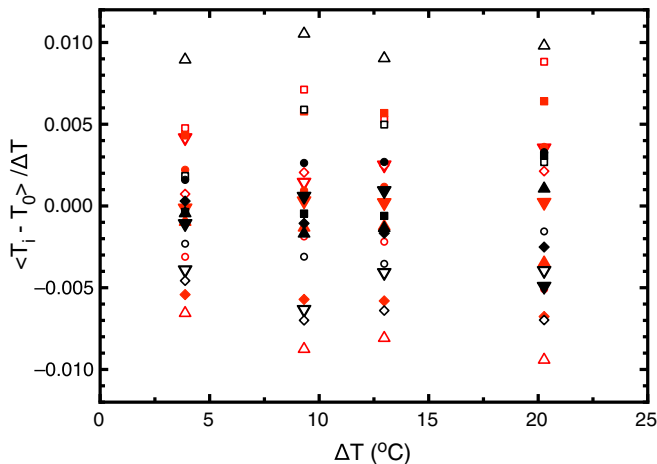


FIG. 5. The spatial variation of the temperature in the top and bottom plates $\langle T_i - T_0 \rangle / \Delta T$. Different symbols represent different plate thermistors. Red symbols: thermistors in the bottom plates. Black symbols: thermistors in the top plates. Solid symbols represent thermistors in the cell we report data from in this paper, while open symbols correspond to data in the adjacent cell. The down-pointing triangle, up-pointing triangle, square, and circle symbols represent the plate thermistors at orientations 0 , $\pi/2$, π , and $3\pi/2$, respectively, while the diamonds correspond to thermistors at the center of their plates. The standard deviation of temperatures in each plate is $0.005\Delta T$.

To determine how much the temperature profile in the top and bottom plates affects the LSC, we switched the flow direction of the temperature-controlled water in the top and bottom plates. Figure 6 shows probability distributions $p(\theta_0)$ in panel (a) and $p(\alpha)$ in panel (b) for forward and reversed flow in the plates, when $\Delta T = 18.35^{\circ}\text{C}$. The peak location of $p(\theta_0)$ shifted by 0.1 rad and the peak of $p(\alpha)$ shifted by 0.2 rad, and even which of the corners the LSC sampled changed (only data from the corner which was sampled by both data sets are shown in Fig. 6). The larger shift in $p(\alpha)$ is a consequence of the larger sensitivity of α to changes in temperature by a factor of 2.3 (Sec. III D). Additionally, $p(\alpha)$ became skewed to one side after the change in flow direction, indicating that nonuniformity in the plate temperature can also change the shape of the distributions. Assuming the standard deviation of plate temperatures of $0.005\Delta T$ extends into the LSC, we estimate $\Delta\theta_0 = 0.005\Delta T / \delta\sqrt{8} = 0.08$ rad for $\Delta T = 18.35^{\circ}\text{C}$, close to the observed shift in the peak of $p(\theta_0)$ in Fig. 6. This confirms that significant effects on $p(\theta_0)$ and $p(\alpha)$ observed in Fig. 6 are due to the nonuniformities in the plate temperatures, and the temperature variation in the plate extends into the LSC.

IV. THE POTENTIAL V_g

A. Relating $V_g(\theta_0)$ to the probability distribution of θ_0

We start our analysis of the potential in one dimension to focus on the four-well potential in θ_0 . For now we ignore α (i.e., set $\alpha = 0$), although we will include α in our analysis starting in Sec. IV B. We test the prediction of the potential $V_g(\theta_0)$ given in Eq. (3) by measuring the probability distribution $p(\theta_0)$. The two are related by the steady-state solution of the Fokker-Planck equation for Eq. (2), assuming overdamped stochastic motion in a potential, and approximating $\delta = \delta_0$, resulting in [44]

$$-\ln p(\theta_0) = \frac{V_g(\theta_0)}{D_{\theta} \tau_{\theta}}. \quad (7)$$

To test this prediction, we searched for a four-peaked $p(\theta_0)$ by carefully leveling the cell. Due to the extreme sensitivity of $p(\theta_0)$ to weak asymmetric forcings mainly from the nonuniformity in the

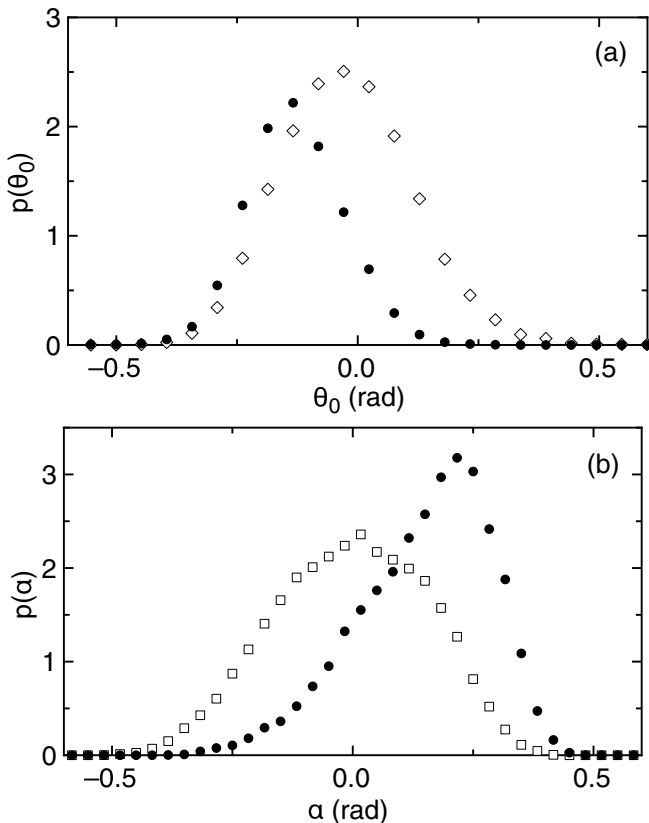


FIG. 6. Probability distributions of (a) θ_0 and (b) α for forward flow (open symbols) and reversed flow (solid symbols) in the cooling channels of the top and bottom plates. The plate temperature distributions significantly affect both the peak location and shape of the probability distributions of θ_0 and α .

plate temperature, we usually find $p(\theta_0)$ is locked mainly in one corner, even when we nominally level the cell (see Fig. 6). To get such a uniform, four-peaked $p(\theta_0)$ required a months-long effort to tune the tilt angle β to just the right value to mostly cancel out other sources of asymmetry. We show a measurement of $p(\theta_0)$ with four peaks in Fig. 7 at $Ra = 4.8 \times 10^8$ and $\beta = 0.0005 \pm 0.0009$ rad. (This is the same data set used in Ref. [46].) Even with the extreme effort to obtain a four-peaked $p(\theta_0)$, these data are not entirely ergodic, as crossings of the LSC orientation from corner to corner only occurred 48 times during the time series, for an average of 12 crossings of each potential barrier and sampling each potential well 12 times, with an approximately $1/\sqrt{12} = 30\%$ error on the relative peaks and minima of $p(\theta_0)$. The corresponding prediction of $p(\theta_0)$ from Eq. (7) is shown for comparison where we used the measured values $D_{\dot{\theta}} = 2.37 \times 10^{-6} \text{ rad}^2/\text{s}^3$ and $\mathcal{T} = 286 \text{ s}$ for a different data set at the same nominal parameter values [46], and fit $\tau_{\dot{\theta}} = 45.5 \text{ s}$ (a factor of 2.6 larger than the measured value at the same nominal parameter values). The comparison indicates that the general shape of the four-peaked $p(\theta_0)$ can be achieved in experiment, although the extreme sensitivity to asymmetries makes this more of a special limiting case than a typical case.

1. Natural frequency ω_r

In anticipation of analytical solutions for oscillation modes, we write an approximation of $V_g(\theta_0)$ in terms of a first-order expansion around each corner for small θ_0 as in Ref. [44]:

$$V_g(\theta_0) \approx \frac{1}{2} \omega_r^2 \theta_0^2 + V_0, \quad (8)$$

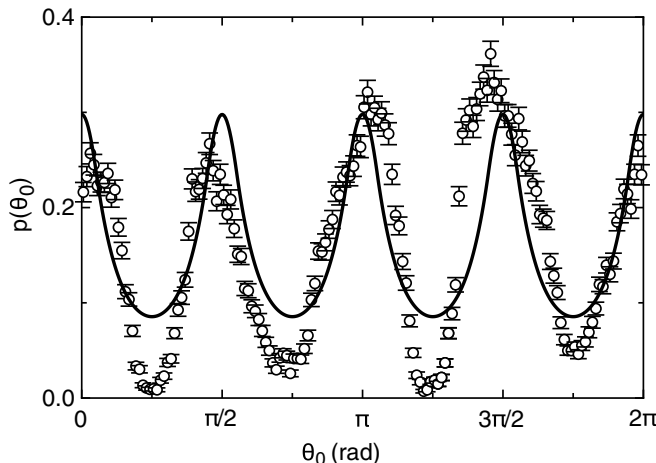


FIG. 7. Circles: A measured probability distribution $p(\theta_0)$ with 4 wells. Solid line: model prediction from Eq. (7) with τ_θ as an adjustable fit parameter. This shows that the predicted four-peaked $p(\theta_0)$ can be obtained in experiments, although it required extreme effort required to carefully tilt the cell to cancel out other sources of asymmetry.

where ω_r corresponds to the natural frequency of oscillations around the potential minimum. ω_r is predicted from Eq. (3) to be [46]

$$\omega_r = \sqrt{\frac{15}{\pi}} \omega_\phi, \quad (9)$$

where $\omega_\phi = 2\pi/\mathcal{T}$ and \mathcal{T} is the turnover time of the LSC. Figure 2 shows the quadratic approximation of the potential in comparison to the full solution.

For a quantitative test of the predicted quadratic potential minimum, we compare to measurements where $p(\theta_0)$ is locked around a single corner. In most of our experiments, we find long intervals where the LSC orientation is locked around a single corner due to the large potential barriers, and further enforce this orientation locking with a standard tilt of the cell by $\beta = 1^\circ$ at $\text{Ra} = 2.62 \times 10^9$. The measured $-\ln p(\theta_0)$ for this case is shown in Fig. 8. We find that the peak of $p(\theta_0)$ is offset slightly from the corner, by 0.05 rad, consistent with the 0.1 rad uncertainty on the peak position due to the nonuniform plate temperature.

To compare the shape of $p(\theta_0)$ to the prediction of Eq. (7), we combine Eq. (7) and Eq. (8) into a fit function and include an offset θ_p to account for the shift in the peak of $p(\theta_0)$ from the corner:

$$-\ln p(\theta_0) = \frac{1}{2} \frac{\omega_r^2}{D_\theta \tau_\theta} (\theta_0 - \theta_p)^2 + \frac{V_0}{D_\theta \tau_\theta}. \quad (10)$$

To obtain the curvature $\omega_r^2/D_\theta \tau_\theta$, we fit Eq. (10) to data in Fig. 8. The input errors for fitting $-\ln p(\theta_0)$ were propagated errors on $p(\theta_0)$ assuming a Poisson distribution, and the fit is reported over the largest range of data which had a reduced $\chi^2 \approx 1$. The fit range of 0.3 rad is shown as the curve in Fig. 8. This range includes 81% of the measured data, and 95% of the data are in a range where the quadratic approximation of the potential from Eq. (8) is within 5% of the exact calculation of $V_g(\theta_0)$ from Eq. (3) (illustrated in Fig. 2). This indicates that the quadratic shape of the potential is correctly predicted within the measurement resolution over the range where most of the data are found. The fit of Eq. (10) to the data in Fig. 8 yields the curvature $\omega_r^2/D_\theta \tau_\theta$, which is multiplied by the measured values of D_θ and τ_θ obtained from data at the same Ra in Figs. 26 and 27 of Appendix A to obtain ω_r .

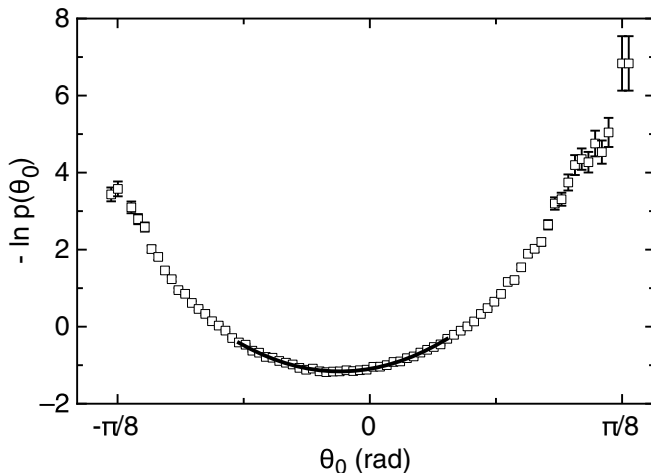


FIG. 8. The probability distribution $p(\theta_0)$ around a single corner, rescaled as $-\ln p(\theta_0)$ to be equal to the predicted dimensionless potential $V_g(\theta_0)/D_\delta \tau_\delta$. Solid line: quadratic fit to the data, indicating agreement with the prediction of Eq. (8).

2. Ra dependence of ω_r

Values of ω_r are obtained by fitting $-\ln p(\theta_0)$ at different Ra. Fits were done with a fixed fit range equal to 2.3 times the standard deviation of the distribution (consistently 80% of the data). For $Ra < 8 \times 10^8$, the reduced χ^2 increases from 1 up to 16 at the lowest Ra, coinciding with an increased asymmetry of the probability distribution around the potential minimum. This indicates an inconsistency with the predicted quadratic probability distribution at lower Ra. The larger χ^2 may result from the increased correlation time of θ_0 at higher Ra [37], which makes the data in $p(\theta_0)$ less independent of each other, and the Poisson distribution a less good approximation for the error.

Values of ω_r are shown as a function of Ra in Fig. 9. The errors on ω_r shown in Fig. 9 include the error on the fits and errors propagated from the scatter of the data of 9.6% on D_δ from Fig. 26 and 3.2% on τ_δ from Fig. 27. For comparison, we also plot the model prediction for the natural frequency ω_r in Fig. 9. The prediction is obtained by plugging in the fit of the measured turnover time \mathcal{T} versus Ra from Fig. 21 below into Eq. (9) to obtain $\omega_r = 7.71 \times 10^{-7} Ra^{0.55 \pm 0.05} \text{ s}^{-1}$. A power-law fit to data for $Ra > 2 \times 10^8$ yields $\omega_r = 3.7 \times 10^{-7} Ra^{0.54 \pm 0.03} \text{ s}^{-1}$, shown in Fig. 9. The errors on the power-law exponent overlap for the prediction and data, indicating consistency with the predicted scaling relation for $Ra > 2 \times 10^8$. The prediction is on average 2.6 times the measured data in this range of Ra. Such an error is typical of this modeling approach [28,37,42], as it makes significant approximations about the shape of the LSC, scale separation between the LSC and small-scale turbulent fluctuations, and the distribution of turbulent fluctuations.

To confirm that the small tilt of $\beta = 1^\circ$ did not bias the data, we applied the same procedure to obtain $\omega_r^2/D_\delta \tau_\delta$ by fitting data at $\beta = 0$ for $Ra = 2.62 \times 10^9$, normalizing the fit curvature of $-\ln p(\theta_0)$ by values of D_δ and τ_δ measured at $\beta = 0$. We found consistent values of ω_r at both tilt angles within the 5% error. On the other hand, the nonuniformity in plate temperature has a significant effect on $p(\theta_0)$; the change in flow direction in the plates shown in Fig. 6(a) caused a 20% change in the fit value of ω_r .

3. Barrier crossing

Other aspects of the shape of the potential are relevant to calculating the rate of the LSC orientation θ_0 crossing a potential barrier ΔV_g from one corner to another. We previously reported

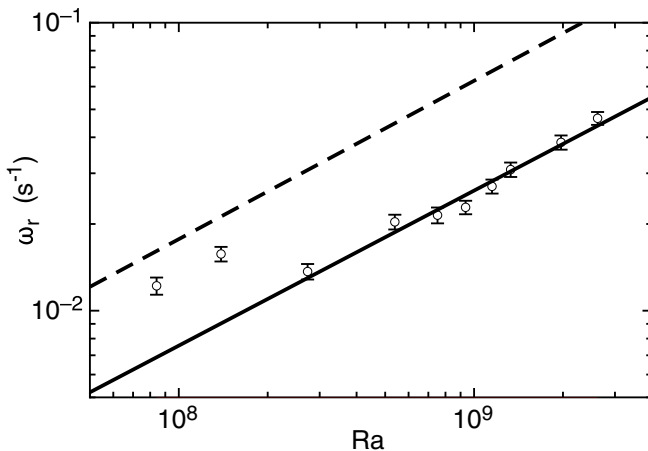


FIG. 9. The natural frequency ω_r of the potential as a function of Ra , obtained from fitting $-\ln p(\theta_0)$. Solid line: power-law fit to the data for $Ra > 2 \times 10^8$. Dashed line: The predicted potential from Eq. (8) using the measured turnover time \mathcal{T} . ω_r scales with the inverse of \mathcal{T} as predicted for $Ra > 2 \times 10^8$, although the magnitude of ω_r is 2.6 times smaller than the prediction in this range.

the overall barrier crossing rate in Ref. [46], and here we show measurements of the geometric parameters used in Kramer's formulation [57]. This requires not only the natural frequency ω_r at the potential minimum, but also a quadratic fit around the maximum of the potential with a corresponding frequency ω_{\max} , and the potential barrier height ΔV_g [46]. These barrier crossing events are nonexistent in most of our data sets, such as those represented in Fig. 8 where the LSC is locked into a narrow range of θ_0 around a single corner due to the tilt of the cell. Instead, ω_{\max} and ΔV_g can be obtained from more ergodic data such as in Fig. 7 where the cell was tilted carefully to make each potential well nearly equally likely. In a previous article, we showed that accurate predictions of the rate of barrier crossing ω could be made using a Kramers' formulation

$$\omega = \frac{\omega_r \omega_{\max} \tau_{\dot{\theta}}}{2\pi} \exp\left(-\frac{\Delta V_g}{D_{\dot{\theta}} \tau_{\dot{\theta}}}\right) \quad (11)$$

where we predicted $\omega_{\max} = \sqrt{3/2} \omega_{\phi}$, $\Delta V_g = (3/8)(1 - \gamma/2)\omega_{\phi}^2$ from Eq. (3), and with values of $\tau_{\dot{\theta}}$, $D_{\dot{\theta}}$, and ω_{ϕ} obtained from independent measurements [46]. Here, we show the intermediate step that relates the parameters ω_{\max} and ΔV_g directly to the potential. To do so, we convert the probability distribution in Fig. 7 to $-\ln p(\theta_0)$ and plot it in Fig. 10. Figure 10 also shows fits of Eq. (10) to data around each potential minimum to obtain $\omega_r^2/D_{\dot{\theta}} \tau_{\dot{\theta}}$, and analogous fits around each potential maximum of

$$-\ln p(\theta_0) = -\frac{1}{2} \frac{\omega_{\max}^2}{D_{\dot{\theta}} \tau_{\dot{\theta}}} (\theta_0 - \theta_{\max})^2 + \frac{V_0 + \Delta V_g}{D_{\dot{\theta}} \tau_{\dot{\theta}}}. \quad (12)$$

To obtain the natural frequencies ω_r and ω_{\max} , the fit curvatures of $\omega_r^2/D_{\dot{\theta}} \tau_{\dot{\theta}}$ and $\omega_{\max}^2/D_{\dot{\theta}} \tau_{\dot{\theta}}$ are multiplied by the measured parameters for $\tau_{\dot{\theta}} = 17.5$ s and $D_{\dot{\theta}} = 2.37 \times 10^{-6}$ rad²/s³ for data at the same nominal parameter values [46], and averaged together for the four fits of each. Averaging over the four minima or maxima helps reduce the bias introduced from the plate temperature nonuniformity, which may affect the curvature of each minimum and maximum differently. This yields $\omega_r = 0.015$ s⁻¹ [three times smaller than the prediction of Eq. (9), similar to Fig. 9], and $\omega_{\max} = 0.046$ s⁻¹ (70% larger than the prediction [46]). The potential barrier ΔV_g was obtained by averaging the values of the fits of Eq. (12), while fixing V_0 to have the same value for the fits of Eqs. (10) and (12), resulting in $\Delta V_g = 1.1 \times 10^{-4}$ s⁻² (30% smaller than the prediction [46]). These

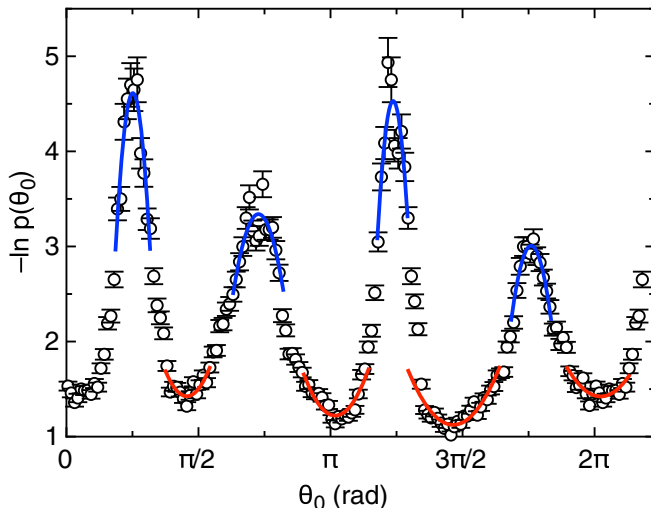


FIG. 10. The measured dimensionless potential $-\ln p(\theta_0)$ when the cell is carefully tilted to cancel most sources of asymmetry. Curves: quadratic fits of the potential minima and maxima to obtain ω_r , ω_{\max} , and ΔV_g .

parameters overestimate the measured barrier crossing rate ω by a factor of 2. This confirms that the relevant quantifiable features of the potential V_g can all be predicted within a factor of 3.

4. Quantitative comparisons of sources of asymmetry

Asymmetries in the dynamics of the LSC are often attributed in part to imperfections in the shape of the container, slight tilt of the cell, temperature profile in the plates, and Earth's Coriolis force [42]. Here we quantitatively compare how large a contribution some of these make to the potential. The largest imperfection in the shape of our flow cell is the epoxy sticking out of the middle wall to protect thermistors by $\Delta D = 0.17$ cm. The predicted potential difference due to this epoxy at its most extreme position relative to the potential difference from the cubic shape is $\Delta V/\Delta V_g \approx 4\Delta D/L = 8\%$. In terms of the dimensionless potential $V/D_{\dot{\theta}}\tau_{\dot{\theta}}$, the change from potential minimum to maximum due to the cubic geometry is $-\Delta \ln p(\theta_0) = 2.6$ based on the average of fits in Fig. 10, so the effect of the wall shape imperfection is expected to be $-\Delta \ln p(\theta_0) = 0.2$. For comparison, the difference due to the change in flow direction in Fig. 6 is $-\Delta \ln p(\theta_0) = 3.3$ at the orientation where the difference is largest, much larger than the wall shape imperfection, and even larger than the effect of the cubic geometry. This explains why in a nominally leveled cell we observed a single-peaked probability distribution of θ_0 instead of four peaks—the plate temperature profile is dominating the potential. Only when we tilted the cell to cancel out most of the effect of the plate temperature nonuniformity did we observe the four-peaked probability distribution.

When we calculate values of ω_r , part of the curvature of $-\ln p(\theta_0)$ we measure might come from the plate temperature nonuniformity, other sources of asymmetry, and nonergodic statistics. Thus, the values we report may be affected by this. For example, the values of ω_r measured at different potential minima in Fig. 10 have a standard deviation of 36%, while the errors on individual fits average 15%. This suggests the other 21% of the variation in measured ω_r comes from asymmetries in the cell, which corresponds to a systematic error in reported values of ω_r from single-corner measurements such as Fig. 8. A similar difference of 20% in ω_r is obtained from data before and after switching the flow direction in the top and bottom plates in Fig. 6, confirming this asymmetry in the measured potential could come from the plate temperature nonuniformity.

B. Generalization of the potential to $V_g(\theta_0, \alpha)$

While the geometry dependence of the potential V_g [(3)] was first introduced as a function of θ_0 [37], and the slosh displacement represented by the angle α is responsible for the sloshing oscillation in circular cylindrical cells [28], the potential has not been calculated as a function of both parameters before. To obtain a potential in terms of both θ_0 and α using the method of Brown and Ahlers [42], we first calculate the horizontal cross-section length $D(\theta_0, \alpha)$ in a square horizontal cross section with displacements in both θ_0 and α as illustrated in Fig. 1(b). This purely geometric calculation is an extension to a previous calculation for a rectangular cell for θ_0 [44], with the additional variable α . A full derivation of the path length $D(\theta_0, \alpha)$ is given in Appendix B. For analytical calculations near corners, where most of the data lie, the expression simplifies in the small angle limit for both θ_0 and α to

$$D(\theta_0, \alpha)^2 \approx 2H^2(1 - |\theta_0 + \alpha| - |\theta_0 - \alpha|). \quad (13)$$

We next convert $D(\theta_0, \alpha)$ to a potential via Eq. (3), which includes smoothing over the width $\gamma = \pi/10$ to account for the finite width of the LSC as in Ref. [44]. To smooth the potential with two parameters, we integrate over the orientations of the hot side of the LSC $\alpha_h = \theta_0 + \alpha$, and the cold side of the LSC $\alpha_c = \theta_0 - \alpha$, as illustrated in Fig. 1. The bounds of the integrals are from $\alpha_h - \gamma/2$ to $\alpha_h + \gamma/2$ on the hot side, and from $\alpha_c - \gamma/2$ to $\alpha_c + \gamma/2$ on the cold side. We change the variables in Eq. (13) to α_h and α_c when substituting into Eq. (3) for the integral, and then change the variables back to θ_0 and α to obtain

$$V_g(\theta_0, \alpha) \approx \frac{15\omega_\phi^2(\alpha^2 + \theta_0^2)}{2\pi} \quad (14)$$

in the limit of small α and θ_0 , and ignoring an additive constant in a potential. This quadratic potential leads to harmonic oscillator solutions to Eq. (2) as a result of the smoothing over the range γ in Eq. (3), with equal curvatures for the potentials in θ_0 and α , and thus equal natural frequencies for oscillations in each variable. This contrasts with the potential for a circular cross section, in which θ_0 does not appear in the potential.

C. $p(\alpha)$

To test the prediction that the potential has the same form in θ_0 and α in the small angle limit, we show $-\ln p(\alpha)$ in Fig. 11 as we did for $-\ln p(\theta_0)$ in Fig. 8, using the same data set as in Fig. 8. Figure 11 shows the potential minimum offset from the corner at 0 by almost 0.2 rad, within the deviation of 0.2 rad found when switching the direction of water flowing through the top and bottom plates in Fig. 6(b). The skewness in $p(\alpha)$ in Fig. 11 is also within the range observed in Fig. 6(b). Thus, these deviations of the peak locations from the corner and asymmetry in $p(\alpha)$ are likely due to the nonuniformity of the plate temperature and are not interpreted to be significant results relevant to the idealized geometry of a cube.

A fit of a quadratic function to $-\ln p(\alpha)$ is shown in Fig. 11 using the same fit range of 0.3 rad as in Fig. 8. This fit range includes 77% of the measured data. The reduced $\chi^2 = 8$ in this fit range using Poisson statistics. This larger χ^2 than for the quadratic fit of $p(\theta_0)$ may be the result of a skewing of $p(\alpha)$ due to the plate temperature nonuniformity, which was found to have a larger effect on α than on θ_0 by a factor of 2.3 (Sec. III D).

The values of ω_r obtained from $p(\theta_0)$ and $p(\alpha)$ are shown in Table I. The curvatures fit in both Figs. 8 and 11 were divided by measured values of $D_\theta \tau_\theta$ from Fig. 26 below to obtain ω_r . The dominant error is due the plate temperature nonuniformity, which was measured from the difference in ω_r obtained from data before and after switching the flow direction in the top and bottom plates in Fig. 6, to be 20% for $p(\theta_0)$ and 40% for $p(\alpha)$. This error may be different for each distribution, so is considered an error for the purposes of comparisons within Table I. In multiplying the curvature of $-\ln p(\theta_0)$ by $D_\theta \tau_\theta$, there is an additional systematic error of 10% on ω_r that is the same for each

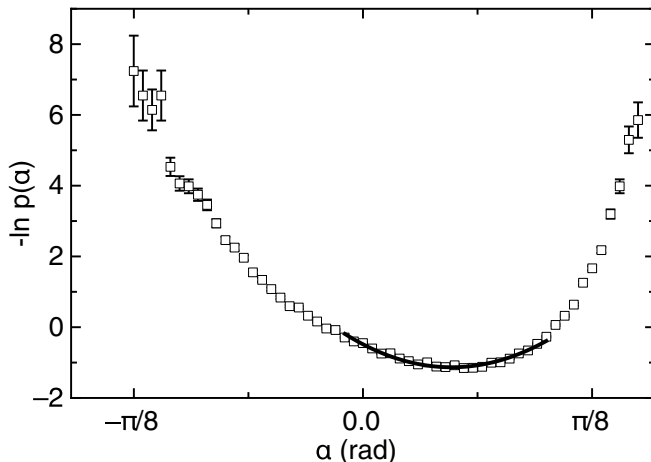


FIG. 11. The probability distribution $p(\alpha)$, rescaled as $-\ln p(\alpha)$ to be equal to the predicted dimensionless potential $V_g(\alpha)/D_\theta \tau_\theta$. Line: quadratic fit using the predicted shape from Eq. (14).

distribution, so is not reported in Table I. The values of ω_r are consistent for $p(\theta_0)$ and $p(\alpha)$ —well within the error from the plate temperature nonuniformity—as predicted from Eq. (14).

D. $p(\theta_0, \alpha)$

To test the quadratic potential approximation in Eq. (14) in both θ_0 and α simultaneously, we calculate the joint probability distribution $p(\theta_0, \alpha)$. We show $p(\theta_0, \alpha)$ in Fig. 12 as a three-dimensional color plot. The joint probability distribution is centered at $\theta_p = -0.06$ rad and $\alpha_p = 0.17$ rad, not at the origin, due mostly to the nonuniform plate temperature profile. As a first approximation, Fig. 12 is close to the circular shape predicted from the quadratic approximation of Eq. (14). However, there appears to be a slight oval shape to the distribution

Since the three-dimensional plot in Fig. 12 only allows for coarse comparisons, we plot slices of the two-dimensional prediction of the potential $V_g(\theta_0, \alpha)$ and compare with the measured probability distributions in Fig. 13. The predictions shown are calculated from the full potential given in

TABLE I. Comparison of the natural frequency ω_r in units of mrad/s obtained from quadratic fits of various projections of the two-dimensional probability distribution $p(\theta_0, \alpha)$. Values are obtained from fits of $-\ln p(\theta_0)$ in Fig. 8 and of $-\ln p(\alpha)$ in Fig. 11, as well as from fits of the negative logarithm of the joint probability distribution $p(\theta_0, \alpha)$ along the four slices of the (θ_0, α) plane shown in Fig. 12. The natural frequency ω_r , and thus the curvature of the potential are consistent along all different slices, in agreement with the predicted quadratic shape of the potential in Eq. (14) and indicate that distributions of θ_0 and α are independent of each other.

Projection	ω_r
$p(\theta_0)$	47 ± 9
$p(\alpha)$	46 ± 18
$p(\theta_0, \alpha = \alpha_p)$	47 ± 9
$p(\alpha, \theta_0 = \theta_p)$	48 ± 19
$p(\theta_0 - \theta_p = \alpha - \alpha_p)$	50 ± 10
$p[\theta_0 - \theta_p = -(\alpha - \alpha_p)]$	41 ± 8

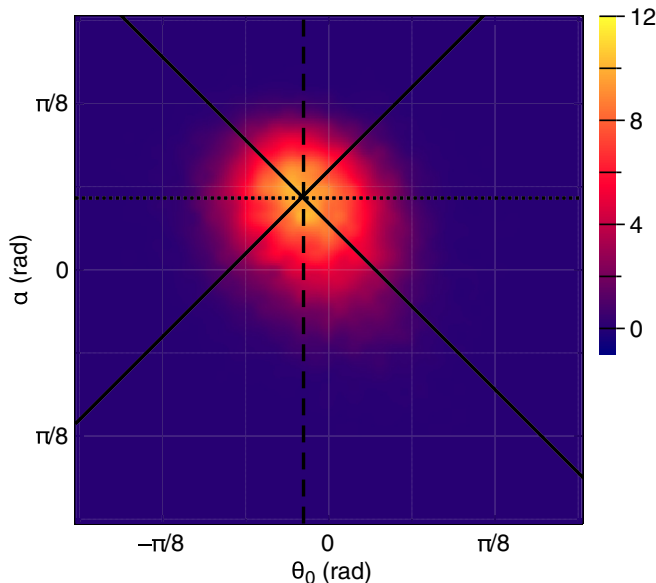


FIG. 12. The joint probability distribution $p(\theta_0, \alpha)$. The distribution is close to the circular shape predicted from the quadratic approximation of Eq. (14), but with a slightly oval shape. The lines indicate slices along which one-dimensional probability distributions are shown in Fig. 13, centered on the peak of the probability distribution at coordinates (θ_p, α_p) .

Appendix B, not the linear approximation in Eqs. (13) and (14), with the natural frequency ω_r a factor of 2.9 smaller than the prediction to fit the potential near the minimum and better compare the shape of the potentials. The prediction of the full potential retains the fourfold symmetry of a cube outside of the linear approximation, although it does not retain azimuthal symmetry around the potential minimum in the θ_0 - α plane at large angles. The local maxima of the potential on any given circle in the θ_0 - α plane centered around the potential minimum are predicted to occur along the θ_0 axis and α axis. The local potential minima on these circles are predicted to be at angles of $\pm 45^\circ$ relative to the θ_0 and α axes, illustrated as the diagonal lines in Fig. 12. The slices of the predicted potential along these lines are shown in Fig. 13.

Measured values of $-\ln p(\theta_0 - \theta_p)$ at $\alpha = \alpha_p$, and $-\ln p(\alpha - \alpha_p)$ at $\theta = \theta_p$ are shown in Fig. 13. These distributions are shifted to be centered around θ_p and α_p to better compare the shapes of the probability distributions to the predicted potential. These distributions are taken as thin slices of the θ_0 - α plane with a width of 0.016 rad. We also plot the measured negative logarithm of the probability distribution along the slices where $\theta_0 - \theta_p = \alpha - \alpha_p$ and $\theta_0 - \theta_p = -(\alpha - \alpha_p)$, corresponding to the diagonal lines shown in Fig. 12. The probability distributions all have similar curvature near the potential minimum, but the tails consistently drop off faster than the predictions. Most of the tails of the measured probability distributions are asymmetric around their centers, likely due to the nonuniform plate temperature or other asymmetries of the setup, so it is difficult to compare the shapes of the measured potentials along different projections.

We fit the quadratic function of Eq. (8) to the four probability distributions shown in Fig. 13, using the same fit range of 0.3 rad as in Figs. 8 and 11, and centered on θ_p and α_p . The fit values are summarized in Table I. All fits have a reduced $\chi^2 \approx 1$, indicating that they are well described by a quadratic function within ± 0.15 rad of the peak, where 80% of the data lies. Furthermore, values of ω_r are consistent with each other along all of the slices of the probability distribution. This indicates the predicted quadratic potential of Eq. (14) is a good qualitative model for $p(\theta_0, \alpha)$ near the potential minimum. Since the fit values of ω_r for the two slices at fixed α and θ_0 are consistent

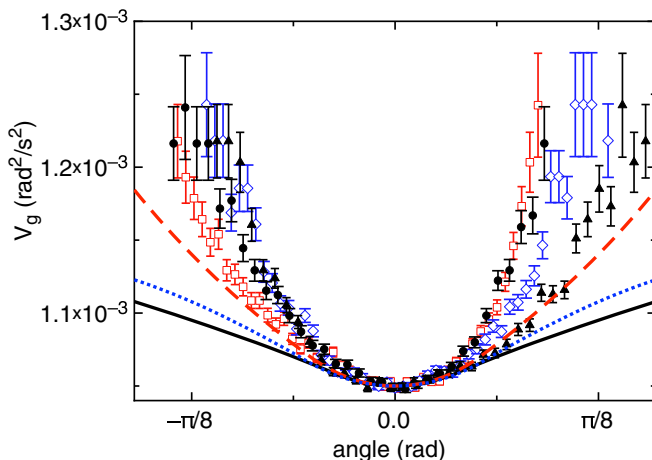


FIG. 13. Comparison of the shape of the predicted potential $V_g(\theta_0, \alpha)$ with the negative logarithm of the measured probability distribution along different slices of the θ_0 - α plane drawn in Fig. 12. Dotted line: predicted potential vs θ_0 . Dashed line: predicted potential vs α . Solid line: predicted potential for $\theta_0 = \alpha$ and $\theta_0 = -\alpha$. All potential predictions are scaled with the natural frequency ω_p , reduced by a factor of 2.9 to fit the measured data near the minimum. Open diamonds: measured $-\ln p(\theta_0)$. Open squares: measured $-\ln p(\alpha)$. Solid triangles and circles: the measured probability distributions along $\theta_0 - \theta_p = -(\alpha - \alpha_p)$ and $\theta_0 - \theta_p = \alpha - \alpha_p$, respectively, corresponding to the solid lines in Fig. 12. The collapse of the data near the potential minimum confirms the form of the potential $V_g \propto \theta_0^2 + \alpha^2$ predicted in Eq. (14).

with the fit results using all of the data, this indicates an independence of the parameters such that distributions of θ_0 are not conditional on α , and distributions of α are not conditional on θ_0 . This confirms that the quadratic potential lacks any coupling terms between θ_0 and α in the small angle limit, which implies the forcing on θ_0 is independent of α [i.e., $-\partial V_g(\theta_0, \alpha)/\partial \theta_0$ is not a function of α], and similarly the forcing on α is independent of θ_0 . This lack of coupling confirms that a correct analysis of the system can be obtained by analyzing it as a function of one parameter at a time.

V. POWER SPECTRUM

A. Model for advected modes

One of the possible dynamical consequences of a potential $V_g(\theta_0, \alpha)$ with a local minimum is oscillations in θ_0 and α around that potential minimum. In circular cylindrical containers, a combination of sloshing and twisting of the LSC structure around the plane of the LSC was found [25–28], where the restoring force for the oscillation came only from the slosh displacement α for a circular cross section. Since a cubic geometry leads to a restoring force in both θ_0 and α , it can potentially excite different modes of oscillation. This section explains the process of calculating the power spectrum for a square cross section from traveling wave solutions of the advected oscillation model of Brown and Ahlers [28] and highlights the differences from a circular cross section.

To obtain equations of motion that account for advection, we start with Eq. (2) for θ_0 with the quadratic potential approximation [(14)], here we also assume the independence of the forcings on θ_0 and α , which is now justified in Sec. IV D. We assume a mathematically similar equation of motion for α , since Eq. (14) has the same quadratic term for both variables.

These equations of motion can be converted into Lagrangian coordinates to view them as traveling waves. Traveling waves can be described in terms of the angles of the hottest spot $\alpha_h = \theta_0 + \alpha$ and coldest spot $\alpha_c = \theta_0 - \alpha$ of the temperature profile in a horizontal cross section and as they travel up and down the walls (illustrated in Fig. 1). In the stationary frame, these traveling

waves superpose to produce our more traditional LSC angles

$$\theta_0 = \frac{\alpha_h + \alpha_c}{2}, \quad \alpha = \frac{\alpha_h - \alpha_c}{2}. \quad (15)$$

To account for advection, we add advective terms to the equations of motion for α_h and α_c , corresponding to upward and downward motion in z , respectively: $\mp(\omega_\phi/k_0)\partial\alpha_{h/c}(z, t)/\partial z$. ω_ϕ/k_0 is the circulation velocity, where k_0 is the wave number corresponding to the circulation. The resulting equation of motion for the upward traveling wave is

$$\ddot{\alpha}_h = -\frac{\dot{\alpha}_h}{\tau_\theta} - \omega_r^2\alpha_h - \frac{\omega_\phi}{k_0}\frac{\partial\dot{\alpha}_h}{\partial z} + f_h(t). \quad (16)$$

Here we have used the approximation $\delta \approx \delta_0$ for simplicity. A similar equation results for the downward traveling wave in terms of α_c , with subscripts h replaced by c , and z replaced by $-z$.

Using the identities of Eq. (15), we convert the equations of motion for the traveling waves, i.e., Eq. (16) and its analogy for α_c back to the stationary frame in terms of θ_0 and α to obtain

$$\ddot{\theta}_0 = -\frac{\dot{\theta}_0}{\tau_\theta} - \omega_r^2\theta_0 - \frac{\omega_\phi}{k_0}\frac{\partial\dot{\alpha}}{\partial z} + f_\theta(t). \quad (17)$$

A similar equation results for α with θ_0 and α transposed. These equations are similar to Eq. (2) but with an additional equation for α , and each equation now has an advective term which couples the equations of motion for θ_0 and α . In contrast, for a circular cross section, the coupling of these equations allowed the restoring force in α to drive oscillations in both α and θ_0 to get the combined sloshing and twisting mode, as no separate restoring force was found for θ_0 in that geometry [28]. In the cube, this coupling is unnecessary to get oscillation of both parameters, as both parameters have their own restoring force due to the minimum in the potential $V_g(\theta_0, \alpha)$ in terms of each parameter.

To find solutions to Eq. (17), we first solve the uncoupled Eq. (16) which has partial solutions in the form of traveling waves given by

$$\alpha_{h,n}(\omega, t) = a_n(\omega) \cos(nk_0z - \omega t - \Phi_n(\omega)) \quad (18)$$

and

$$\alpha_{c,n}(\omega, t) = a_n(\omega) \cos[-nk_0z - \omega t - \Phi_n(\omega) + \psi_n], \quad (19)$$

where z is the height of the thermistor rows relative to the midplane, $\Phi_n(\omega)$ accounts for any phase shifts between different frequencies or modes, and ψ_n is a phase shift between the upward- and downward-traveling waves. If plumes making up the LSC remain coherent over multiple turnover times, they can destructively interfere with each other when they loop around. To satisfy the condition for constructive interference for a closed loop circulation, where α_h and α_c are two different segments of the same traveling wave, requires $\psi_n = (n+1)\pi$ with integer n , and the coefficients $a_n(\omega)$ and phases $\Phi_n(\omega)$ be the same for both α_h and α_c . Since there is a restoring force for both θ_0 and α , nontrivial solutions are expected for all positive integers n . In contrast, for a circular cross section there is only a restoring force for α , producing only even- n order modes [28]. Summing these traveling wave solutions for α_h and α_c using the identities in Eq. (15) results in standing waves in the lab frame given by

$$\theta_{0,n}(\omega, t) = a_n(\omega) \cos(nk_0z) \cos[\omega t - \Phi_n(\omega)] \quad (20)$$

and

$$\alpha_n(\omega, t) = a_n(\omega) \sin(nk_0z) \sin[\omega t - \Phi_n(\omega)] \quad (21)$$

for odd n . The sines and cosines are switched for even order n solutions. Plugging in these standing wave solutions with the time dependence represented as a complex exponential into Eq. (17) as a

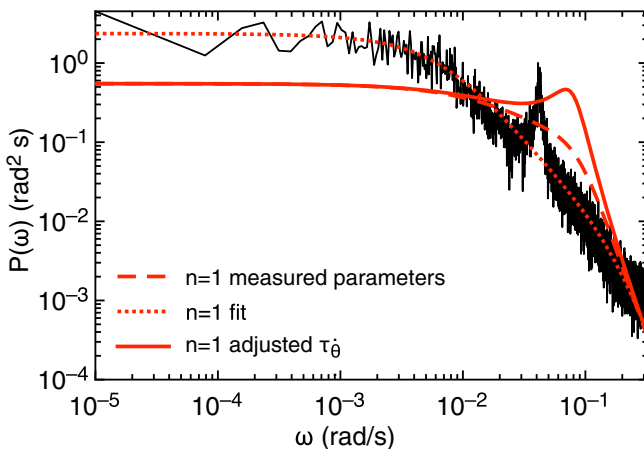


FIG. 14. Power spectrum of θ_0 . Black curve: measured data. Red dashed curve: prediction using measured values of $D_{\dot{\theta}}$, $\tau_{\dot{\theta}}$, \mathcal{T} , and ω_r and $n = 1$ as input. This prediction captures the plateau of the power spectrum but is in the overdamped regime of the model where there is no resonance peak. Red dotted curve: fit to the data. The fit parameters are all within a factor of about 2 of independently measured values, but do not include a resonance peak. Red solid curve: using the same measured values for input data as the red dashed curve but scaling $\tau_{\dot{\theta}}$ up by a factor of 2.3 to fit the resonant frequency as a function of Ra. This small change in parameter values is enough to move the model from an overdamped to underdamped state, with resonance near the observed peak frequency, indicating that the model is consistent with the *observed* oscillation. However, the uncertainties on parameter values are too large to make correct *predictions* that the system is in the underdamped state rather than the overdamped state.

function of frequency ω and assuming $f(t)$ is described by white noise with diffusivity $D_{\dot{\theta}}$ yields the power spectrum of θ_0 at $z = 0$ for a given mode of integer order n :

$$P_n(\omega) = |a_n(\omega)|^2 = \frac{D_{\dot{\theta}}}{(\omega^2 - \omega_r^2 - n\omega\omega_{\phi})^2 + \left(\frac{\omega}{\tau_{\dot{\theta}}}\right)^2}. \quad (22)$$

While there is an infinite series of modes for integer n , the $n = 1$ mode is expected to be the dominant mode, since higher-frequency modes tend to have less peak power due to the larger magnitude of damping at higher frequency.

B. Testing the power spectrum

To test the prediction of the power spectrum $P_1(\omega)$, we show an example in Fig. 14 of the measured power spectrum for $\text{Ra} = 2.62 \times 10^9$ and $\beta = 1^\circ$. The power spectrum has a roll-off indicative of damping, and a peak which corresponds to a resonant frequency for oscillations. The corresponding probability distribution in Fig. 8 confirms that these oscillations are nearly centered around a corner, as predicted.

To test the self-consistency of a stochastic ODE model to describe the power spectrum, we calculate a prediction for $P_1(\omega)$ for the expected dominant $n = 1$ mode from Eq. (22), using the measured value of ω_r obtained from fitting $p(\theta_0)$ (Sec. IV), along with the independently measured \mathcal{T} , $D_{\dot{\theta}}$, $\tau_{\dot{\theta}}$ (Appendix A) and the definition $\omega_{\phi} = 2\pi/\mathcal{T}$. This prediction of $P_1(\omega)$ is shown as the red dashed curve in Fig. 14. The low-frequency plateau is about a factor of 3 away from the measured plateau. The resonant peak is missing for these parameter values, although there is some power above the background near the natural frequency, which is within 9% of the measured oscillation frequency. While the prediction is in the ballpark of the measured power spectrum, the parameter values are in a range such that the model does not predict the observed resonance peak.

To determine what model parameter range could be consistent with the data, we fit the predicted functional form of the power spectrum $P_1(\omega)$ from Eq. (22) to the measured $P(\omega)$, assuming a constant error (to balance out the higher logarithmic density of data at lower probability), and fixing $n = 1$. The fit yields $D_{\dot{\theta}} = (3.9 \pm 5.2) \times 10^{-6} \text{ rad}^2/\text{s}^3$, $\tau_{\dot{\theta}} = 5.7 \pm 3.6 \text{ s}$, $\omega_{\phi} = 0.066 \pm 0.045 \text{ rad/s}$, and $\omega_r = 0.036 \pm 0.012 \text{ rad/s}$. This fit is shown as the red dotted curve in Fig. 14. The large errors are a consequence of having more free parameters than distinct features in the background, and the parameters being strongly coupled to each other. For comparison, the values from measurements of the mean-square displacement and turnover time are $D_{\dot{\theta}} = (2.68 \pm 0.26) \times 10^{-6} \text{ rad}^2/\text{s}^3$, $\tau_{\dot{\theta}} = 13.3 \pm 0.4 \text{ s}$, $\omega_{\phi} = 0.049 \pm 0.003 \text{ rad/s}$ from Appendix A, and $\omega_r = 0.047 \pm 0.009 \text{ rad/s}$ from measurements of $p(\theta_0)$ in Sec. IV. The fitted parameter values are in general within a factor of about 2 of the measured values, which confirms some amount of self-consistency of the stochastic ODE model within these generous errors that the model has required in some cases [37]. While these parameters fit the background well, this fit still does not capture the peak of the power spectrum in Fig. 14. This is because the model overestimates the width of the peak, so a least-squares fit results in a better fit by fitting only the background and ignoring the peak.

The linearized model of Eq. (22) also failed to capture the peak of the power spectrum of θ_0 in a circular cylinder [28]. In that case, the discrepancy could be attributed to the variable damping in the original model due to the variation of δ in the damping term of Eq. (2) [37]. Modeling the damping as random effectively reduces the damping by a factor to $1 - S$ where $S = (\sigma_{\delta}/\delta_0)^2 \tau_{\delta}/\tau_{\dot{\theta}}$, and $\sigma_{\delta} = \sqrt{D_{\delta}} \tau_{\delta}$ is the standard deviation of δ in the linearized limit of Eq. (1) [28]. This correction could move the state of the system from the overdamped to the underdamped regime if the damping adjustment S is large enough. For this transition to occur for our measured parameter values from Appendix A at $\text{Ra} = 2.62 \times 10^9$ requires $S > 0.47$. However, we calculate S ranging from 0.01 to 0.16 as Ra decreases from 2.62×10^9 to 8.41×10^7 using the measured parameter values from Appendix A. This is not enough of a correction to move the system to the underdamped regime. This is a much smaller correction factor in a cube compared to the $S = 0.5$ reduction found at higher Ra in a circular cylinder [28]. This smaller correction is mostly a consequence of the smaller relative fluctuation strength σ_{δ}/δ_0 for this data set relative to that of Ref. [28], also the reason cessations are much less likely for these data [46].

To show how close the parameter values are to the underdamped regime, starting with the measured parameters values, we increase $\tau_{\dot{\theta}}$ to a factor of 2.3 times the measured value to move the system into the underdamped regime, shown as the red solid curve in Fig. 14. The system is near enough to the overdamped-underdamped transition that a change in parameter values by a factor of about 2 can cross this transition and qualitatively change the dynamics. While this variation in parameter values is consistent with typical errors of the model, this means that these uncertainties on parameter values are too large for the model to correctly predict the observation that the system is in the underdamped state rather than the overdamped state.

While $n = 1$ is predicted to be the advected mode with the most peak power, the predicted dropoff in peak power averages about 30% for each integer increase in n (not shown) when using the measured parameter values $D_{\dot{\theta}}$, and ω_r , and increasing $\tau_{\dot{\theta}}$ by a factor of 2.3 to obtain resonance. Higher order modes are not resolvable in the steep and noisy rolloff of the measured data in Fig. 14.

VI. OSCILLATION STRUCTURE

In this section, we characterize the oscillation structure and compare it to model predictions of how it differs from oscillations in other cell geometries such as twisting and sloshing in cells with circular cross section [25–28] or rocking in horizontal cylinders [44]. We characterize the oscillation structure by phase shifts in correlation functions between orientations or slosh angles at different rows of thermistors [28].

Detailed predictions for the phase shifts of the correlation functions from the standing-wave solutions of Eqs. (21) and (20) are shown in Appendix C. The predicted structure for the expected dominant $n = 1$ mode is an oscillation where θ_0 is in phase at all rows of thermistors, similar to

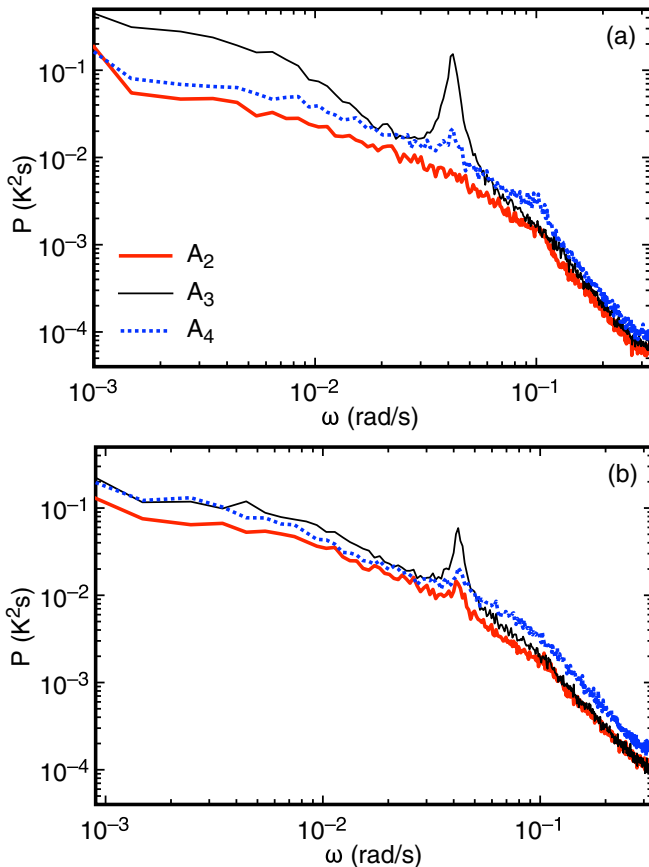


FIG. 15. The power spectra of the Fourier modes A_n of the temperature profile for (a) the middle row of thermistors and (b) bottom row of thermistors. Red thick solid line: A_2 . Thin black solid line: A_3 . Blue dotted line: A_4 . Each signal has a peak at the same frequency as the oscillation in θ_0 except for A_2 at the middle row. This differs qualitatively from circular cylinders, where only A_2 was found to oscillate. Oscillations in A_2 at the top and bottom row only in the primary peak correspond to the predicted $n = 1$ mode. Weaker higher-frequency peaks in A_2 at all rows correspond to the predicted $n = 2$ mode.

that found in a tilted circular cylinder [42], and α is out of phase at the top and bottom rows, corresponding to an LSC rocking back and forth around the horizontal axis in the LSC plane, similar to the rocking mode found in a horizontal cylinder [44].

A. Power spectra of A_n

Before showing correlation functions to identify the oscillation structure, we show power spectra of the Fourier moments A_n of the temperature profile to identify which of these Fourier moments contribute to oscillation structure, and thus which A_n should be considered in calculating correlation functions and phase shifts. Power spectra of the Fourier moments A_n of the temperature profile from Eq. (6) are shown in Fig. 15(a) for the middle row thermistors and Fig. 15(b) for the bottom row. The top row power spectrum is not shown since we find it to be qualitatively similar to the bottom row, following the symmetry of the Boussinesq approximation. Each signal except for A_2 at the middle row has a primary peak at $\omega = 0.44$ rad/s, the same frequency as the oscillation in θ_0 (Fig. 14).

Since α is calculated from A_2 (Sec. III D), the oscillation of A_2 in Fig. 15 at the top and bottom rows, but not at the middle row ($z = 0$) at the primary frequency, is consistent with the predicted

$n = 1$ sloshing mode [(21)]. This oscillation is distinct from the $n = 2$ mode in a circular cylindrical cell where A_2 oscillates at all three rows [28].

The oscillations in A_3 and A_4 in Fig. 15 were not found in circular cylinders [28]. A_4 contributes to a shift in the extrema of the temperature profile closer together, thus could also be interpreted as contributing to a sloshing oscillation. The peak in A_3 causes a shift in both extrema of the temperature profile in the same direction, so does not contribute to sloshing, but could be affect the interpretation of the LSC orientation. The moment A_3 is the dominant oscillating mode in Fig. 15, and even has more power than the oscillation θ_0 (comparing the integral of the peaks in Fig. 15 with Fig. 14). A_3 corresponds to an oscillation of the shape of the temperature profile that appears to be induced by the oscillation of θ_0 around the corners of the cubic cell, which will be discussed in detail in a follow-up paper [56].

Smaller, secondary peaks are observed in the power spectra in Fig. 15 at about twice the frequency of the $n = 1$ mode, where the $n = 2$ mode is expected. Observed oscillations in A_2 and A_4 at all three rows correspond to the sloshing component of the $n = 2$ mode, and the oscillations in A_3 at the top and bottom rows, but not the middle row, could correspond to the twisting component of the $n = 2$ mode. These observations are in agreement with the expectations that this $n = 2$ mode that has been found in circular cylinders [28] is still expected to occur in a cube at approximately twice the frequency of the $n = 1$ mode [42], but with less power than the lower-frequency $n = 1$ mode due to increased damping at higher frequency.

B. Definition of modified oscillation angles $\hat{\theta}_0$ and $\hat{\alpha}$ for measuring phase shifts

Since A_3 and A_4 were not found to oscillate in a circular cylindrical cell [28], they were not used in the original definitions of θ_0 or α . Since A_3 and A_4 could be interpreted as contributing to a the LSC orientation or slosh angle, respectively, we consider alternate definitions of the LSC orientation and slosh angle when calculating correlation functions that include these higher-order Fourier modes. We assume that the orientations of the maximum $\hat{\alpha}_h$ and minimum $\hat{\alpha}_c$ of the temperature profile (5) are the relevant orientations as far as oscillations are concerned. The modified oscillation angles are defined as $\hat{\theta}_0 = (\hat{\alpha}_h + \hat{\alpha}_c)/2$ and $\hat{\alpha} = (\hat{\alpha}_h - \hat{\alpha}_c)/2$ in analogy to Eq. (15), where A_3 contributes to $\hat{\theta}$, and both A_2 and A_4 contribute to $\hat{\alpha}$. For consistency with previous work, we have used the previous definitions of θ_0 and α in Secs. IV, V, and A. We confirmed that the values of ω_r in Sec. IV, for example, vary by only 20% (within systematic errors) if $p(\hat{\theta}_0)$ is used to calculate ω_r instead of $p(\theta_0)$.

C. Definition of correlation functions

The correlation function between two signals $x(t)$ and $y(t)$ is defined as

$$C_{x,y}(\tau) = \frac{\langle (x(t) - \bar{x})(y(t - \tau) - \bar{y}) \rangle}{\sqrt{\langle (x(t) - \bar{x})^2 \rangle \langle (y(t) - \bar{y})^2 \rangle}}, \quad (23)$$

where both $\langle \dots \rangle$ and \bar{x} denote time averages. x and y can stand for the angles θ_m , θ_t , and θ_b , which correspond to θ_0 at the middle, top, and bottom rows of thermistors, respectively, and the angles α_m , α_t , and α_b , which correspond to α at the middle, top, and bottom rows, respectively, or the modified versions of those angles.

D. Measured correlation functions and comparison with prediction

In this subsection, we show the five independent cross-correlation functions where we found the most clear oscillations to measure all the phase shifts between the six independent time series of angles (orientation and slosh angles at three rows each).

Figure 16 shows the cross-correlations $C_{\hat{\theta}_b, \hat{\theta}_m}$ and $C_{\hat{\theta}_t, \hat{\theta}_m}$. Since both signals in Fig. 16 have evenly spaced peaks with the same spacing, then $\hat{\theta}_m$, $\hat{\theta}_b$, and $\hat{\theta}_t$ are all oscillating at the same frequency. Since $C_{\hat{\theta}_b, \hat{\theta}_m}$ and $C_{\hat{\theta}_t, \hat{\theta}_m}$ have peaks near $\tau = 0$, then $\hat{\theta}_t$, $\hat{\theta}_b$, and $\hat{\theta}_m$ are all in phase with each other.

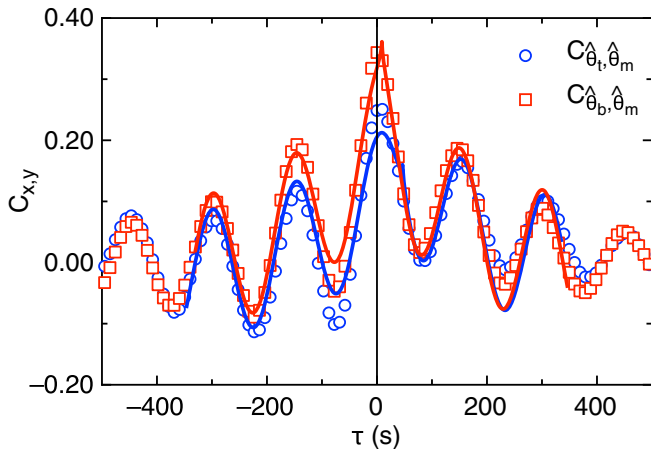


FIG. 16. Cross-correlations between the modified LSC orientation $\hat{\theta}_0$ of different rows of thermistors, as indicated in the legend. Lines: fits of Eq. (24) to data of the same color to determine the phase shifts between signals and frequency of oscillation. The alignment of the peaks at $\tau = 0$ indicates that $\hat{\theta}_t$, $\hat{\theta}_b$, and $\hat{\theta}_m$ are oscillating in phase with each other, in agreement with the predicted $n = 1$ advected oscillation mode.

The positive correlations indicate the three rows tend to line up in a vertical plane. This in-phase oscillation in $\hat{\theta}_0$ is in agreement with the predicted $n = 1$ advected oscillation mode described in Appendix C and distinct from the $n = 2$ twisting oscillation found in circular cylinders [25,28].

The phase shift of $\hat{\theta}_0$ is dominated by the A_3 Fourier mode, which has the same phase at all three rows of thermistors. θ_0 at the top and bottom rows is also in phase with $\hat{\theta}_0$, however θ_0 at the middle row is found to be out π rad of phase with the top and bottom rows and the A_3 mode. These different phase shifts for different definitions of the LSC orientation indicate a more complex oscillation structure than predicted, which we will follow up on in a later paper [56].

Figure 17 shows phases shifts between α at different rows with θ_m to determine the phase shifts between different rows of α . The extrema of C_{α_b, θ_m} and C_{α_t, θ_m} have phases of approximately $\pi/2$ rad with opposite signs, corresponding to α_b and α_t oscillating π rad out of phase with each other. Regardless of which angle definitions we use, we find α_b and α_t are π rad out of phase with each other. The out-of-phase behavior of α_b and α_t is consistent with the $n = 1$ oscillation mode prediction in Appendix C, again distinct from the $n = 2$ mode found in circular cylindrical containers in which the different rows of α oscillate in phase with each other [26–28].

The equally spaced peaks in C_{α_m, θ_m} in Fig. 17 indicate that α_m is also oscillating at the same frequency as other modes, however, this is not expected as part of the $n = 1$ mode. The oscillation in α_m is much weaker than α_t and α_b , as there was no resolvable peak in the power spectrum of A_2 in Fig. 15(a). The weak oscillation in α_m that is π rad out of phase with θ_m corresponds to a weak sloshing on top of the θ_0 oscillation such that α_c oscillates with a slightly larger amplitude than α_h . This asymmetry between α_h and α_c appears to be a new non-Boussinesq effect and not an asymmetry of the setup (see Appendix D for justification).

VII. OSCILLATION PERIOD

To test whether the model can make quantitative predictions of the oscillation period and whether the system is overdamped or underdamped, we compare predictions and measurements at different Ra.

We show examples of measured autocorrelations C_{θ_m, θ_m} at different Ra in Fig. 18. With decreasing Ra, the oscillation amplitude in the correlation function decreases. For $Ra = 2.73 \times 10^8$ or lower, we could not clearly resolve any oscillation.

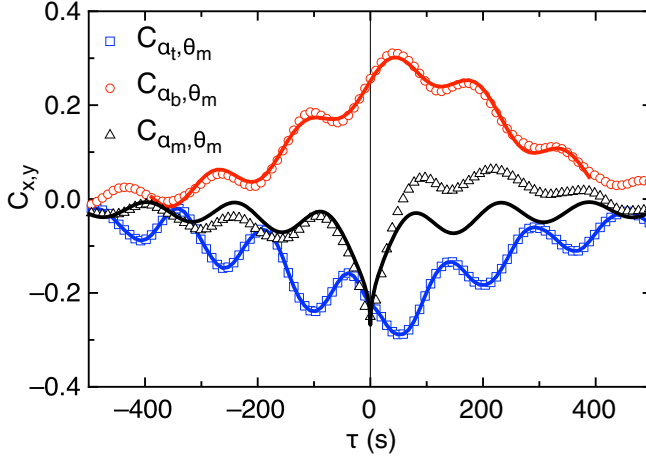


FIG. 17. Cross-correlations between α at different rows of thermistors with θ_m , as indicated in the legend. Lines: fits of Eq. (24) to data of the same color to determine the phase shifts between signals and frequency of oscillation. The approximately $\pi/2$ rad phase shifts and opposite signs of C_{α_b, θ_m} and C_{α_t, θ_m} indicate that α_b and α_t are oscillating π rad out of phase with each other, consistent with the $n = 1$ mode. The oscillation in α_m is not part of the $n = 1$ mode, but indicates an asymmetry between the hot and cold sides of the LSC.

To quantitatively calculate the oscillation period T_{osc} from cross-correlation functions, we used the fit function

$$C_{x,y}(\tau) = b_1 \cos\left(\frac{2\pi}{T_{\text{osc}}}\tau - \phi_{x,y}\right) + b_2 e^{-|\frac{\tau-b_3}{b_4}|^{b_5}} + b_6. \quad (24)$$

The fits of Eq. (24) are shown along with the cross-correlations in Figs. 16, 17, and 18. The parameters b_2 through b_6 are for fitting a decaying background which is not analyzed here. The input error for the fit is a constant adjusted to get a reduced $\chi^2 = 1$. Values of $\phi_{x,y}$ are generally consistent with reported phase shifts in Sec. VID. We report the average T_{osc} from the five correlation functions reported in Sec. VID for each Ra. Error bars represent the uncertainties on the fits.

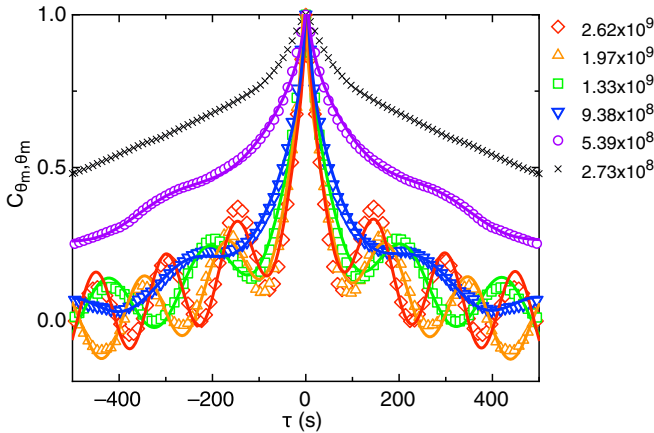


FIG. 18. The autocorrelation C_{θ_m, θ_m} for different Ra given in the legend. We did not observe any oscillation for $Ra \leq 2.73 \times 10^8$.

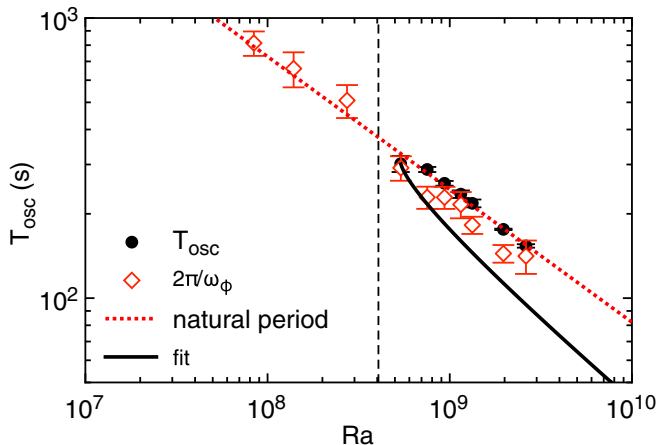


FIG. 19. Solid circles: The measured oscillation period T_{osc} as a function of Ra . Vertical dashed line: Ra below which oscillations disappeared. Solid line: model prediction using the measured values of ω_r , \mathcal{T} , and adjusting $\tau_{\hat{\theta}}$ by a factor of 2.3 larger than the measured value to fit data. Dotted line: the natural period of the potential. Open diamonds: measured turnover time. The oscillation period is consistent with both the natural period of the potential and the turnover time.

The prediction for the oscillation period T_{osc} is calculated numerically as the frequency of the maximum of the power spectrum in Eq. (22) for $n = 1$, since the $n = 1$ mode is predicted to be the dominant mode and the oscillation structure observed from the correlation functions in Sec. VID is consistent with the $n = 1$ mode. We used fits from Sec. IV for the measured Ra dependence of ω_r , from Appendix A for \mathcal{T} and $\tau_{\hat{\theta}}$, and adjusted $\tau_{\hat{\theta}}$ by a constant factor to best fit the data in Fig. 19. This fit is shown as the solid line in Fig. 19. The average magnitude of the difference between the fit and data is 28% of the measured value, using a fit value of $\tau_{\hat{\theta}}$ larger than the measured value by a factor of 2.3. The major constraint in the fit was to obtain the critical Ra_c where oscillations disappear, so the agreement with the measured T_{osc} is an indication that the natural frequency ω_r obtained from $p(\theta_0)$ also describes the oscillations, which confirms the self-consistency of the stochastic ODE model. This same adjustment of $\tau_{\hat{\theta}}$ also allowed capturing the peak in the power spectrum of θ_0 (red solid curve in Fig. 14). While this suggests that the model is reasonably consistent with the data within its large error, this error is still large enough to span the overdamped-underdamped transition such that the model cannot correctly predict the observation that the system is the underdamped state rather than the overdamped state.

A significant consequence of advection in the model is that it eliminates the usual diverging trend of the resonant period near the overdamped-underdamped transition of a damped harmonic oscillator, producing oscillations closer to the natural frequency until the overdamped-underdamped transition is reached.

A. Possible alternate interpretations of the scaling of oscillation period

We note that in the range of Ra where we observe oscillations, the oscillation period is within 2% and within error of the natural frequency $2\pi/\omega_r$ (dotted line in Fig. 19), corresponding to the limiting solution where ω_r is dominant in Eq. (22). The oscillation period is also close the turnover period (open diamonds in Fig. 19), larger by an average of 16% in the range of Ra where the oscillation is found, about equal to the 12% systematic uncertainty on \mathcal{T} . Such a close agreement is expected for the $n = 1$ advected mode in the limit where advection is the dominant factor in determining the oscillation frequency. Either limiting solution may be appropriate for the model depending on parameter values.

The fact that the resonant period T_{osc} is close to \mathcal{T} is also consistent with an alternate model where the oscillation is driven more directly by the turnover of the LSC—perhaps by a periodic driving force [58], rather than being driven by white noise with frequency determined by the curvature of the potential and advection. Such a periodic driving force driven at the turnover frequency could lead to the good agreement of the resonant period with the turnover time in the underdamped regime, and still have a transition to overdamping, as observed in Fig. 19. It could also lead to the sharper peak in the power spectrum near the turnover period observed in Fig. 14. Since the measured period is close to the turnover time and the prediction of Eq. (22), we cannot distinguish if one interpretation is more correct than the other or if a combination of both mechanisms exist in this geometry. Nonetheless, we emphasize a useful feature of the Brown and Ahlers model is that it can correctly predict different dynamics in different geometries, specifically that the predicted and observed $n = 2$ oscillation mode in a circular cross-section cell has twice the frequency of the LSC turnover [28], while the predicted and observed $n = 1$ mode in a cubic cell has the same frequency as the LSC turnover.

VIII. SUMMARY AND CONCLUSIONS

The model of Brown and Ahlers [42] was able to correctly predict the four-well shape of the geometry-dependent potential $V_g(\theta_0)$ for a cubic cell (Fig. 7). This includes the quadratic shape of the potential minima $V_g(\theta_0, \alpha)$ near the corners with equal curvatures in both θ_0 and α , indicating they are independent (Figs. 8, 11, 12, and 13 and Table I). The natural frequency ω_r was found to scale with the inverse of the turnover time \mathcal{T} at higher Ra as predicted, although the prediction was larger than measurements by factor of 2.9 (Fig. 9), which is a typical error of this model [37]. The magnitudes of the curvature of the potential near its peak, as well as the potential barrier height, which are relevant to barrier crossing events, were both predicted accurately within a factor of 2 (Fig. 10). Such errors are typical of this modeling approach [28,37,42], as it makes significant approximations about the shape of the LSC, scale separation between the LSC and small-scale turbulent fluctuations, and the distribution of turbulent fluctuations.

Oscillation modes centered around corners of the cubic cell were observed above a critical $\text{Ra} = 4 \times 10^8$, which appears in the model as a crossing of an underdamped-overdamped transition. Above this critical Ra, the oscillation period is consistent with the natural period of the potential and the turnover time (Fig. 19). The value of the critical Ra, as well as frequency and background of the power spectrum of θ_0 are consistent with the measured one if the model parameters ω_r , \mathcal{T} , $\tau_{\dot{\theta}}$, and $D_{\dot{\theta}}$ were adjustable up to a factor of 2.3 away from independently measured values, or a factor of 3 from predicted values (Figs. 14 and 19), again typical errors of this model [37]. However, this uncertainty in the model parameters turns out to be too large to correctly predict whether the system is in its underdamped or overdamped state, as the dynamics are sensitive to the model parameters near the overdamped-underdamped transition.

The structure of these oscillations is mainly the predicted $n = 1$ advected oscillation mode, consisting of out-of-phase oscillations in the top and bottom rows of thermistors of the slosh angle α (i.e., a rocking mode) and in-phase oscillations in all three rows of the modified LSC orientation $\hat{\theta}_0$ (Figs. 16 and 17). This mode is distinct from the $n = 2$ twisting and sloshing mode predicted and observed in a circular cylindrical cell [28]. The $n = 1$ advected oscillation mode exists in cubic cells because of a restoring force due to the variation of the diameter $D(\theta_0)$ across the cube around a corner [42]. A weaker $n = 2$ advected oscillation mode is also observed in the cubic cell, as predicted by the model. Weak oscillations in α_m in phase with the oscillation in θ_m correspond to breaking of the Boussinesq symmetry where the cold side of the LSC oscillates with a larger amplitude than the hot side (Fig. 17). There are hints of a more complex oscillation structure involving a higher order Fourier moments A_n of the temperature profile (Fig. 15) which will be addressed in a follow-up work.

We consider it remarkable that a low-dimensional model of diffusive motion in a potential can predict many features of a high-dimensional turbulent flow. Nontrivial predictions that were confirmed include the shape of the potential as a function of cell geometry, and the successful

prediction of a how the oscillation structure changes with the cell geometry. The ability of this model to predict how features of the LSC dynamics change from a circular to square cross-section containers suggests that such a model could be applied more generally to predict dynamics for different cross-section shapes supporting a single convection roll. Since the modeling approach assumes a robust large-scale structure with a scale separation from small-scale turbulent fluctuations, it is not limited to Rayleigh-Bénard convection, there is great promise for general models of the dynamics of large-scale coherent structures in turbulent flows. Extending predictions to multiple convection roll systems and more complex convection roll shapes remain open problems. While the model has been able to predict features within about a factor of 2, the sensitivity of features near the overdamped-underdamped transition to model parameters leads to an inability to predict correctly whether the system will oscillate or not (even though the observations are consistent with the model within the generous errors). For this modeling approach to be useful in predicting such sensitive features will require more refinement of the quantitative accuracy of the predictions by allowing more complex functions in the model, as was done by [43].

ACKNOWLEDGMENTS

We thank the University of California, Santa Barbara machine shop, and K. Faysal for helping with construction of the experimental apparatus. This work was supported by Grant CBET-1255541 of the US National Science Foundation.

APPENDIX A: MEASUREMENTS OF MODEL PARAMETER VALUES

In this Appendix, we report independent measurements of the parameters that are input into Eqs. (1), (2), and (3) using mainly the methods of Ref. [37], so that these parameters can be used to test model predictions in Secs. IV, V, and VII. Measurements reported in this section were done with a time step of 2.16 s to capture faster fluctuations of the LSC.

1. Turnover time

In Ref. [59], the LSC turnover time was calculated from the peak of the cross-correlation between two thermistors mounted on the opposite sides of the side wall. However, in our case, the same calculation yields suspiciously low turnover times and a correlation peak with the opposite sign as in a circular cylinder [59]. This suggests this correlation time may be affected by the different oscillation modes of the LSC structure which change with the cell geometry. Therefore, we took a different approach in this paper to obtain the turnover time using information from more thermistors.

We measured the correlation times of thermistor pairs vertically separated by $H/4$ and along the path of the LSC. As is illustrated in Fig. 20(b), there are four such pairs in the two columns of thermistors most closely aligned with the mean path of the LSC. The correlation between each pair is shown in Fig. 20(a). We fitted a Gaussian function to data near each peak, as shown in Fig. 20(a). We took the average of those four peak locations as the time the LSC needed to travel the distance $H/4$, with a standard deviation of the mean of 10%. While we do not know the specific path length of the LSC, it can be reasonably bounded between an oval with path length $\pi(1 + \sqrt{2})/2H$ and a rectangle with path length $2(1 + \sqrt{2})H$, and so we take the mean of those two paths of $\lambda = 4.3H$ as our best estimate of the path length of the LSC, with a 12% uncertainty spanning to the two extremes. The turnover time \mathcal{T} was then calculated as the correlation time between the two vertically separated thermistors scaled up by the path length λ divided by $H/4$. The resulting turnover time \mathcal{T} for different Ra is shown in Fig. 21. The error on \mathcal{T} was obtained as the standard deviation of the mean of the fit propagated in quadrature with the error from the uncertainty on the path length. A power-law fit to the data yields $\mathcal{T} = 1.8 \times 10^7 \text{Ra}^{-0.55 \pm 0.05}$.

The Grossmann-Lohse model gives the scaling between Re and Ra as $\text{Re} = 0.31\text{Ra}^{4/9}\text{Pr}^{-2/3}$ when fit to similar data in the same Ra and Pr range in circular cylindrical containers [59]. For the cubic cell, we calculate the Reynolds number as $\text{Re} = \lambda H / \mathcal{T} \nu$. The resulting prediction for the

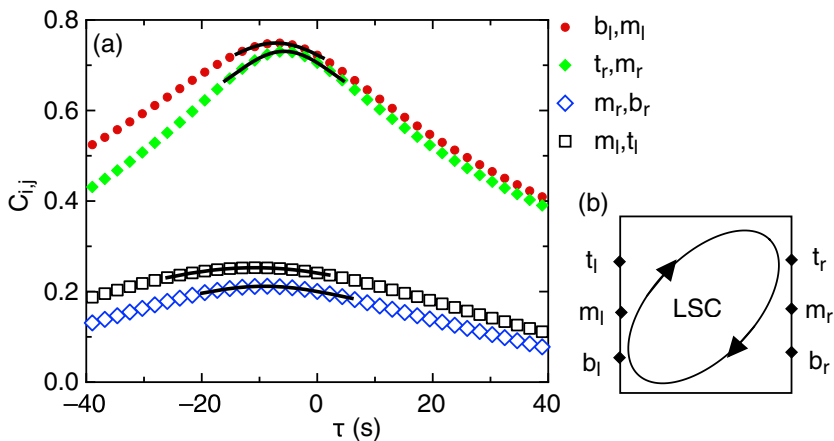


FIG. 20. (a) The correlation function between thermistor temperatures vertically separated by $H/4$ along the path of the LSC. The thermistors correlated in each case are indicated in the legend. Lines: Gaussian fits to the peak of each data set. (b) Illustration of the path of the LSC and thermistor labels.

turnover time $\mathcal{T} = 4.3H^2/(\nu\text{Re}) = 2.1 \times 10^6\text{Ra}^{-4/9}$ is shown as the dashed line in Fig. 21. The prediction is consistent with the error of the data indicating that the Re-Ra relations for cubic and circular cylindrical cells are consistent with each other within the 16% error of the data.

2. Stable fixed-point temperature amplitude δ_0

To present measurements of the stable fixed point temperature amplitude δ_0 in a general form, we make use of the model that was used to derive Eq. (1) [37], which predicted a relationship between δ_0 and the Reynolds number to be

$$\frac{\delta_0\text{Ra}}{18\pi\Delta T\text{Pr}} = c\text{Re}^{3/2}, \quad (\text{A1})$$

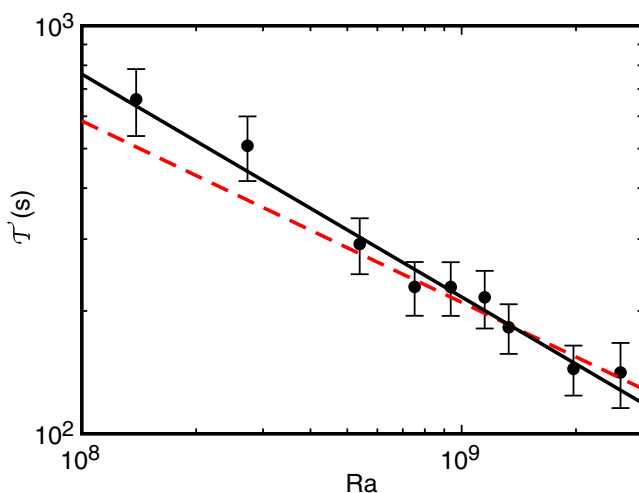


FIG. 21. The turnover time \mathcal{T} as a function of Ra. Solid line: a power-law fit. Dashed line: prediction of the Grossmann-Lohse model, which is consistent with the data.

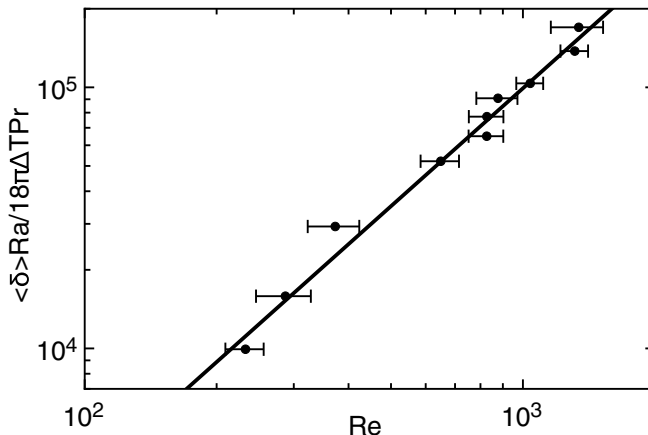


FIG. 22. The mean temperature amplitude $\langle \delta \rangle$ scaled as in Eq. (A1) as a function of Re . Solid line: power-law fit to $cRe^{3/2}$. The scaling is consistent with the prediction of Eq. (A1), and both the scaling and value of fit coefficient c are consistent with those found in circular cylindrical cells.

where c is a dimensionless fit coefficient of order 1. We approximate $\delta_0 \approx \langle \delta \rangle$, since $p(\delta)$ is nearly symmetric around its stable fixed point δ_0 [37]. We plot $\langle \delta \rangle$ scaled according to the left side of Eq. (A1) as a function of Re in Fig. 22. We calculate $Re = UH/\nu$ where U is the ratio of the distance $H/4$ between vertically separated thermistors and the correlation time calculated in Appendix A 1, with an error propagated from the standard deviation of the mean of the correlation time. We fit the data in Fig. 22 to Eq. (A1) with c as the only free parameter, which yields $c = 3.13 \pm 0.14$ with a reduced $\chi^2 = 0.5$. This prefactor is consistent within a couple of standard deviations of $c = 2.8 \pm 0.1$ obtained in a circular cylinder [37], indicating that the same relationship holds between δ_0 and Re in both geometries.

3. Diffusivity and damping time of the temperature amplitude δ

The diffusivity D_δ and damping time τ_δ were obtained by measuring the mean-square change of the temperature amplitude $\langle (d\delta)^2 \rangle$ over a time period dt . The diffusive behavior of the noise in Eq. (1) leads to the prediction $\langle (d\delta)^2 \rangle = D_\delta dt$ for small dt [37]. We fit $\langle (d\delta)^2 \rangle = D_\delta dt$ to data within the range of $0.25\tau_\delta \leq dt \leq 0.6\tau_\delta$ to obtain D_δ [37]. An example is shown in Fig. 23(a). The data do not follow the diffusive trend very well, indicating that Eq. (1) does not capture the short time fluctuations of δ very well. Nonetheless, Eq. (1) has been found to capture the qualitative dynamics of δ in circular cylindrical cells [37], as the dynamics of stochastic ordinary differential equations are often not very sensitive to the details of the fluctuation distributions, and we still use the fit to obtain a value for D_δ . Different fit ranges could result in different values of D_δ , and in the worst case, our fit range overestimates D_δ by as much as a factor of 2. Fits are of similar quality at different Ra .

Equation (1) leads to the prediction $\langle (d\delta)^2 \rangle = 2D_\delta\tau_\delta$ in the limit of large time dt , assuming small variations in δ such that the net forcing in Eq. (1) is approximately linear in δ near the stable fixed point δ_0 [37]. The damping time τ_δ was obtained from fitting the plateau value of $\langle (d\delta)^2 \rangle = 2D_\delta\tau_\delta$ in the limit of large time dt after the value of D_δ was determined [37]. An example is shown in Fig. 23(a). While τ_δ could be underestimated by as much as a factor of 2 due to the poor fit of the diffusive scaling at short times, the plateau value $2D_\delta\tau_\delta$ and thus the variance of δ are still well defined by this fit.

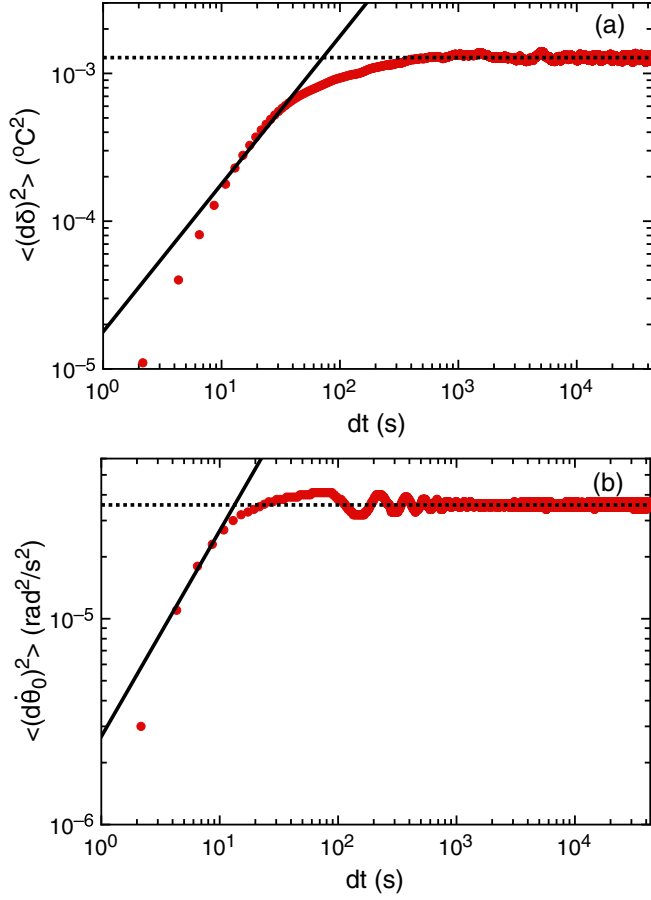


FIG. 23. The mean-square change (a) $\langle (d\delta)^2 \rangle$ and (b) $\langle (d\dot{\theta}_0)^2 \rangle$ as a function of the time interval dt . Solid lines: linear fits to the data for small dt yield the diffusivities D_δ and $D_{\dot{\theta}}$, respectively. Dotted line: constant fits to data for large dt yield τ_δ and $\tau_{\dot{\theta}}$, respectively.

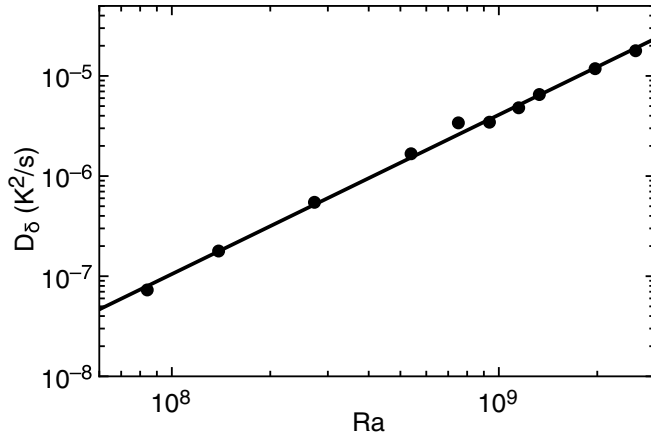


FIG. 24. Measurement of the diffusivity D_δ as a function of Ra . Solid line: power-law fit, which yields $D_\delta \propto Ra^{1.59 \pm 0.03} \text{K}^2/\text{s}$, different from the scaling found in a circular cylindrical cell.

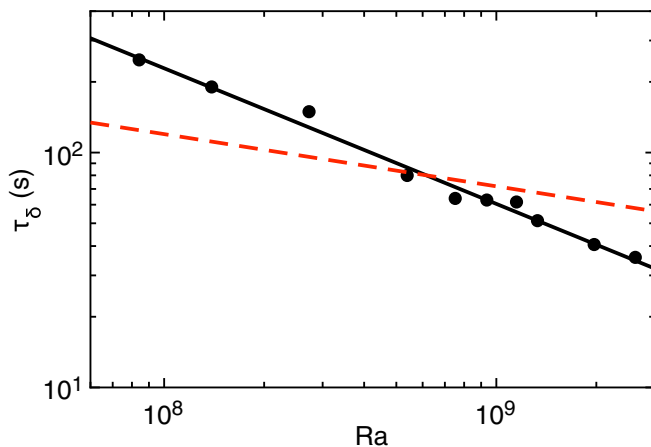


FIG. 25. Measurement of the damping time τ_δ as a function of Ra. Solid line: power-law fit, which yields $\tau_\delta \propto \text{Ra}^{-0.58 \pm 0.02}$ s, different from the scaling found in a circular cylindrical cell. Dashed line: prediction of Ref. [37].

The Ra dependence of D_δ is shown in Fig. 24. A power-law fit yields $D_\delta = 2.0 \times 10^{-20} \text{Ra}^{1.59 \pm 0.03}$ K²/s with a standard deviation between the data and fit of 9.3%. This scaling differs from that found in a circular cylindrical cell $D_\delta \propto \text{Ra}^{1.96}$ at higher Ra [37].

The Ra dependence of τ_δ is shown in Fig. 25. A power-law fit yields $\tau_\delta = 9.5 \times 10^6 \text{Ra}^{-0.58 \pm 0.02}$ s with a standard deviation between the data and fit of 7.1%. Reference [37] predicted that $\tau_\delta = H^2/18\nu\text{Re}^{1/2}$ [37]. Using the GL model for Re, the prediction is $\tau_\delta = 7.2 \times 10^3 \text{Ra}^{-2/9}$ s in our range of Ra. This prediction is shown in Fig. 25. While the prediction has a different scaling exponent than the data, the magnitude of the prediction is within a factor of 2 over the measured range. The scaling also differs from that found in a circular cylindrical cell $\tau_\delta \propto \text{Ra}^{-0.43}$, in which case the model also only predicted the correct order of magnitude [37]. As in a circular cylindrical cell, we also find the scaling of the measured $\tau_\delta \propto \text{Ra}^{-0.58 \pm 0.02}$ [37] is consistent with the scaling of the turnover time $\mathcal{T} \propto \text{Ra}^{-0.55 \pm 0.05}$.

4. Diffusivity and damping time of the angular rotation rate $\dot{\theta}_0$

The diffusivity $D_{\dot{\theta}}$ and damping timescale $\tau_{\dot{\theta}}$ were calculated from the mean-square change of $\dot{\theta}_0$ similar to δ , where $\langle (d\dot{\theta}_0)^2 \rangle = D_{\dot{\theta}} dt$ was fit for small dt and $\langle (d\dot{\theta}_0)^2 \rangle = D_{\dot{\theta}} \tau_{\dot{\theta}}$ was fit for large dt . An example is shown in Fig. 23(b). This assumes small variations in $\dot{\theta}_0$ such that the forcing on $\dot{\theta}_0$ in Eq. (2) is approximately linear in $\dot{\theta}_0$ —more specifically, the incremental change in rotation rate from the potential term $\nabla V_g(\theta_0) dt$ is small compared to the contribution from diffusion $\sqrt{D_{\dot{\theta}}} dt$ and damping $\dot{\theta}_0 \delta dt / \tau_{\dot{\theta}} \delta_0$ for small dt [37]. The validity of this approximation is confirmed by the parameter values reported in this section.

The Ra dependence of $D_{\dot{\theta}}$ is shown in Fig. 26, the power-law fit yields $D_{\dot{\theta}} = 3.2 \times 10^{-13} \text{Ra}^{0.74 \pm 0.03}$ rad²/s³ with a standard deviation between the data and fit of 9.6%. The scaling is consistent with that found in a circular cylinder $D_{\dot{\theta}} \propto \text{Ra}^{0.76}$ rad²/s³.

The Ra dependence of $\tau_{\dot{\theta}}$ is shown in Fig. 27. A power-law fit yields $\tau_{\dot{\theta}} = 2.7 \times 10^4 \text{Ra}^{-0.35 \pm 0.01}$ s with a standard deviation between the data and fit of 3.2%. Brown and Ahlers predicted that $\tau_{\dot{\theta}} = H^2/2\nu\text{Re}$ [37]. Using the GL model for Re, the prediction is $\tau_{\dot{\theta}} = 2.5 \times 10^5 \text{Ra}^{-4/9}$ s, which has a different power-law exponent, but is within a factor of 2 of the data in the range of Ra tested. The scaling also differs from that found in a circular cylindrical cell $\tau_{\dot{\theta}} \propto \text{Ra}^{-0.20}$, in which case the model also only predicted the correct order of magnitude [37].

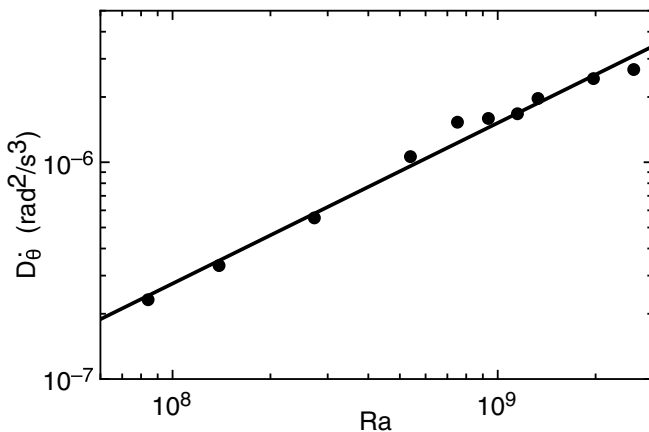


FIG. 26. Measurement of the diffusivity D_{θ} as a function of Ra . Solid line: power-law fit, which yields $D_{\theta} \propto Ra^{0.74 \pm 0.03} \text{ rad}^2/\text{s}^3$, different from the scaling found in a circular cylindrical cell.

5. Applicability of model parameters to other experiments or simulations

While the parameter values presented here in Appendix A are useful for analyzing this experiment, care should be taken when comparing to other experiments or simulations under different conditions, as not all appropriate scalings are known.

Tilt of the cell relative to gravity could change parameter values. There is a significant effect of tilt on D_{θ} . When increasing from $\beta = 0$ to $\beta = 2^\circ$, D_{θ} was found to decrease by 18% per degree, so our reported data at $\beta = 1^\circ$ have a smaller D_{θ} than at $\beta = 0$ by 18%. The values of τ_{θ} , τ_{δ} , and D_{δ} were within measurement errors at different tilt angles up to $\beta = 2^\circ$.

While the spatial variation of plate temperature affected the preferred orientation of the LSC, the variation of plate temperature over time could in principle lead to apparent increases in the diffusivities. Correlations between thermistors in the plates and in the middle row of the sidewall are less than 7% at the highest $\Delta T = 18.35^\circ\text{C}$ (where the plate temperature fluctuations are strongest)

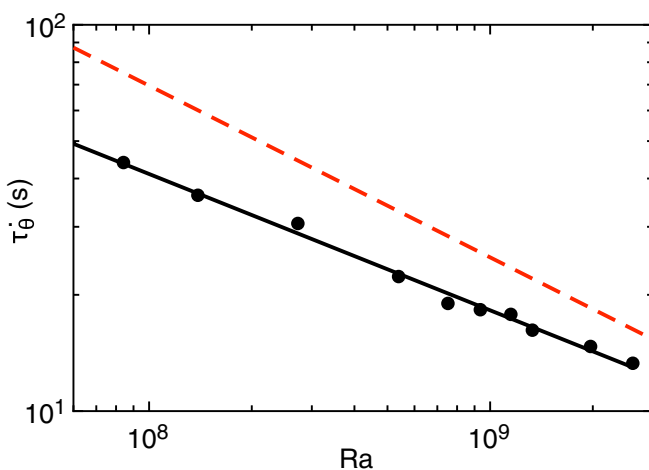


FIG. 27. Measurement of the damping time τ_{θ} as a function of Ra . Solid line: power-law fit, which yields $\tau_{\theta} \propto Ra^{-0.35 \pm 0.01} \text{ s}$, different from the scaling found in a circular cylindrical cell. Dashed line: prediction of Ref. [37].

for time delays less than τ_{δ} where fluctuations are dominant in the dynamics, suggesting that effects of the plate temperature fluctuations on D_{δ} are less than 7%.

APPENDIX B: CALCULATION OF $D(\theta_0, \alpha)$

To calculate $D(\theta_0, \alpha)$ using the geometry shown in Fig. 1(b), we label the center of the cube as O , the location on the wall at the hot side of the LSC as A , and the location on the wall at the cold side of the LSC as B . The length of line OA is

$$\overline{OA} = \frac{\frac{\sqrt{2}}{2}H}{|\cos(\theta_0 + \alpha)| + |\sin(\theta_0 + \alpha)|}. \quad (\text{B1})$$

Similarly, the length of line OB is

$$\overline{OB} = \frac{\frac{\sqrt{2}}{2}H}{|\cos(\theta_0 - \alpha)| + |\sin(\theta_0 - \alpha)|}. \quad (\text{B2})$$

The length of the third side of the triangle of AOB —which corresponds to $D(\theta_0, \alpha)$ —is calculated using the law of cosines to be

$$D(\theta_0, \alpha)^2 = \overline{OA}^2 + \overline{OB}^2 - 2\overline{OA}\overline{OB}\cos(\pi - 2\alpha). \quad (\text{B3})$$

Substituting Eqs. (B1) and Eq. (B2) into this expression for $D(\theta_0, \alpha)$ yields

$$D(\theta_0, \alpha)^2 = \frac{H^2}{2} \{ [|\cos(\theta_0 + \alpha)| + |\sin(\theta_0 + \alpha)|]^{-2} + [|\cos(\theta_0 - \alpha)| + |\sin(\theta_0 - \alpha)|]^{-2} + 2\cos 2\alpha [|\cos(\theta_0 + \alpha)| + |\sin(\theta_0 + \alpha)|]^{-1} [|\cos(\theta_0 - \alpha)| + |\sin(\theta_0 - \alpha)|]^{-1} \}. \quad (\text{B4})$$

For analytical calculations near corners, this expression simplifies in the small angle limit for both θ_0 and α to

$$D(\theta_0, \alpha)^2 \approx 2H^2(1 - |\theta_0 + \alpha| - |\theta_0 - \alpha|). \quad (\text{B5})$$

APPENDIX C: PREDICTION OF OSCILLATION MODES AND PHASE SHIFTS $\phi_{x,y}$ FOR THE ADVECTED OSCILLATION MODEL

In this Appendix, we give detailed predictions for the phase shifts $\phi_{x,y}$ in correlation functions. These are predicted from the model by evaluating the correlation functions of Eq. (23) in terms of the standing-wave partial solutions $\alpha_n(\omega, t)$ and $\theta_{0,n}(\omega, t)$ from Eqs. (21) and (20). Since these are functions of frequency ω , the correlation function is integrated over $d\omega$ to cover all frequencies. Averaging over time first and using the identity $P_n(\omega) = |a_n(\omega)|^2$ results in simplified expressions which identify specific phase shifts $\phi_{x,y}$ for each cross-correlation. We address cases for different angle pairs x, y and odd and even n in this Appendix.

For modes with odd- n order and correlations between different rows of θ_0 , the predicted correlation function is $C_{\theta_i, \theta_j}(\tau) \propto \cos(nk_0z_i) \cos(nk_0z_j) \int P_n(\omega) \cos(\omega\tau) d\omega$ where i and j correspond to the top, middle, or bottom rows of thermistors. As long as the power spectrum $P_n(\omega)$ has a resonance peak (as seen in Fig. 14), the integral produces an oscillatory function in τ with a period the same as the resonant period of $P_n(\omega)$. Since $\cos(\omega\tau)$ has a peak at $\tau = 0$, the integral also has a peak at a time delay $\tau = 0$, corresponding to a phase shift $\phi_{\theta_i, \theta_j} = 0$. When $\cos(nk_0z_i) > 0$, the overall correlation is positive. This occurs, for example, at the middle row where $z_i = 0$, and for $n = 1$ at the top and bottom rows for the value of $k_0 = \pi/2H$ in an aspect ratio 1 circular cylinder [28] or $k_0 = \pi/[1 + \sqrt{2}]H$ in a cube. Thus, the predicted structure for the dominant $n = 1$ mode is an oscillation where θ_0 is in phase at all rows, similar to that found in a tilted circular cylinder [42].

For modes with odd- n order and correlations between different rows of α , the predicted correlation function is $C_{\alpha_i, \alpha_j}(\tau) \propto \sin(nk_0z_i) \sin(nk_0z_j) \int P_n(\omega) \cos(\omega\tau) d\omega$. The integral again is

an oscillatory function in τ as long as $P_n(\omega)$ has a resonance peak and has a peak at a time delay $\tau = 0$, corresponding to a phase shift $\phi_{\alpha_i, \alpha_j} = 0$. However, the sign of the correlation now varies with the row chosen. For example, when calculating $C_{\alpha_b, \alpha_i}(\tau)$, then $z_i = -z_j$, so the product $\sin(nk_0z_i)\sin(nk_0z_j)$ is negative for all odd n , resulting in a negative correlation. For correlations with the middle row at $z = 0$, the corresponding sinusoid in front of the integral is 0, resulting in no oscillation. These correspond to a predicted oscillation in α where the top and bottom rows are out of phase, corresponding to an LSC rocking back and forth around the horizontal axis in the LSC plane, similar to the rocking mode found in a horizontal cylinder [44].

For cross correlations between θ_0 and α , the predicted correlation function is $C_{\alpha_i, \theta_j}(\tau) \propto -\cos(nk_0z_j)\sin(nk_0z_i) \int P_n(\omega) \sin(\omega\tau) d\omega$. The integral again is an oscillatory function in τ as long as $P_n(\omega)$ has a resonance peak, but now with a peak near $\omega\tau = \pi/2$ for a phase shift of $\pi/2$. If $\cos(nk_0z_i) > 0$ (e.g., at the middle row, or for modes $n = 1$ and $n = 3$ at the top and bottom rows), then the cosine term is positive and the sign of the correlation is determined by the row of α . The correlation between θ_m with α_t is negative since $\sin(nk_0z_i) < 0$, while the correlation between θ_m with α_b is positive since $\sin(nk_0z_i) > 0$. For correlations with the middle row of α at $z = 0$, the corresponding sinusoid in front of the integral would again be 0, resulting in no oscillation.

For modes with even- n order, the places of θ_0 and α are switched from the odd n calculation in this subsection. For the $n = 2$ mode, this reproduces the result found in circular cylinders, with an out-of-phase (twisting) oscillation in θ_0 , and in-phase (sloshing) oscillation in α [28].

APPENDIX D: NON-BOUSSINESQ EFFECTS RESULTING IN ASYMMETRY OF THE OSCILLATION

The oscillation in α_m that is π rad out of phase with θ_m shown in Fig. 17 corresponds to an asymmetry in which α_c oscillates with a larger amplitude than α_h . This appears to be a non-Boussinesq effect in which a difference in material parameters at different temperatures on the hot and cold sides of the LSC leads to different local effective values of model parameters that affect the motion of α_h and α_c [for example, the parameters ω_r , D_δ and τ_δ in Eq. (16)].

To test whether this asymmetry is a non-Boussinesq effect rather than due to some other asymmetry of the system, we compare the distributions of α_h and α_c when the flow direction has aligned with a different corner of the cell, since different results from corner to corner would come from asymmetries of the setup. Using the dataset that sampled all four potential wells from Fig. 7, we calculate root-mean-square values of α_h and α_c for each well. For each corner, we find $\alpha_{c,rms} > \alpha_{h,rms}$. The means \pm standard deviations of the four distributions are $\langle \alpha_{h,rms} \rangle = 0.32 \pm 0.07$ rad and $\langle \alpha_{c,rms} \rangle = 0.44 \pm 0.06$ rad. This corresponds to a systematically larger variation of α_c by 36%. This systematic difference is apparently a non-Boussinesq effect due to the temperature difference of the hot and cold sides. The variation in $\alpha_{h,rms}$ and $\alpha_{c,rms}$ of 0.06 or 0.07 rad are much larger than the expected random variation for thousands of measurement points in each well, which could correspond to an asymmetry of the experimental setup. Alternatively, this asymmetry could be due to a lack of ergodicity in which the system does not sample different asymmetric solutions long enough to cancel out those asymmetries in the average, although our primary data set where this asymmetry was observed was 10 days long.

While the appearance of this non-Boussinesq oscillation mode may be of interest in its own right, since it does not have the symmetry between the hot and cold sides of the LSC of the idealized model we are testing in this paper, it will not be discussed further here.

[1] E. N. Lorenz, Deterministic nonperiodic flow, *J. Atmos. Sci.* **20**, 130 (1963).

[2] E. Brown and G. Ahlers, Large-Scale Circulation Model of Turbulent Rayleigh-Bénard Convection, *Phys. Rev. Lett.* **98**, 134501 (2007).

-
- [3] A. de la Torre and J. Burguete, Slow Dynamics in a Turbulent Von Kármán Swirling Flow, *Phys. Rev. Lett.* **99**, 054101 (2007).
- [4] S. Thual, A. J. Majda, and S. N. Stechmann, A stochastic skeleton model for the MJO, *J. Atmos. Sci.* **71**, 697 (2014).
- [5] G. Rigas, A. S. Morgans, R. D. Brackston, and J. F. Morrison, Diffusive dynamics and stochastic models of turbulent axisymmetric wakes, *J. Fluid Mech.* **778**, R2 (2015).
- [6] P. Holmes, J. L. Lumley, G. Berkooz, and C. W. Rowley, *Turbulence, Coherent Structures, Dynamical Systems, and Symmetry* (Cambridge University Press, Cambridge, 2012).
- [7] G. Ahlers, S. Grossmann, and D. Lohse, Heat transfer and large-scale dynamics in turbulent Rayleigh-Bénard convection, *Rev. Mod. Phys.* **81**, 503 (2009).
- [8] D. Lohse and K.-Q. Xia, Small-scale properties of turbulent Rayleigh-Bénard convection, *Annu. Rev. Fluid Mech.* **42**, 335 (2010).
- [9] R. Krishnamurti and L. N. Howard, Large scale flow generation in turbulent convection, *Proc. Natl. Acad. Sci. USA* **78**, 1981 (1981).
- [10] E. Brown and G. Ahlers, Rotations and cessations of the large-scale circulation in turbulent Rayleigh-Bénard convection, *J. Fluid Mech.* **568**, 351 (2006).
- [11] H.-D. Xi and K.-Q. Xia, Cessations and reversals of the large-scale circulation in turbulent thermal convection, *Phys. Rev. E* **75**, 066307 (2007).
- [12] F. Heslot, B. Castaing, and A. Libchaber, Transition to turbulence in helium gas, *Phys. Rev. A* **36**, 5870 (1987).
- [13] M. Sano, X. Z. Wu, and A. Libchaber, Turbulence in helium-gas free convection, *Phys. Rev. A* **40**, 6421 (1989).
- [14] B. Castaing, G. Gunaratne, F. Heslot, L. Kadanoff, A. Libchaber, S. Thomae, X. Z. Wu, S. Zaleski, and G. Zanetti, Scaling of hard thermal turbulence in Rayleigh-Bénard convection, *J. Fluid Mech.* **204**, 1 (1989).
- [15] S. Ciliberto, S. Cioni, and C. Laroche, Large-scale flow properties of turbulent thermal convection, *Phys. Rev. E* **54**, R5901 (1996).
- [16] T. Takeshita, T. Segawa, J. A. Glazier, and M. Sano, Thermal Turbulence in Mercury, *Phys. Rev. Lett.* **76**, 1465 (1996).
- [17] S. Cioni, S. Ciliberto, and J. Sommeria, Strongly turbulent Rayleigh-Bénard convection in mercury: Comparison with results at moderate Prandtl number, *J. Fluid Mech.* **335**, 111 (1997).
- [18] X. L. Qiu, S. H. Yao, and P. Tong, Large-scale coherent rotation and oscillation in turbulent thermal convection, *Phys. Rev. E* **61**, R6075 (2000).
- [19] X. L. Qiu and P. Tong, Onset of coherent oscillations in turbulent Rayleigh-Bénard convection, *Phys. Rev. Lett.* **87**, 094501 (2001).
- [20] J. Niemela, L. Skrbek, K. R. Sreenivasan, and R. J. Donnelly, The wind in confined thermal turbulence, *J. Fluid Mech.* **449**, 169 (2001).
- [21] X. L. Qiu and P. Tong, Temperature oscillations in turbulent Rayleigh-Bénard convection, *Phys. Rev. E* **66**, 026308 (2002).
- [22] X. L. Qiu, X. D. Shang, P. Tong, and K.-Q. Xia, Velocity oscillations in turbulent Rayleigh-Bénard convection, *Phys. Fluids* **16**, 412 (2004).
- [23] C. Sun, K. Q. Xia, and P. Tong, Three-dimensional flow structures and dynamics of turbulent thermal convection in a cylindrical cell, *Phys. Rev. E* **72**, 026302 (2005).
- [24] Y. Tsuji, T. Mizuno, T. Mashiko, and M. Sano, Mean Wind in Convective Turbulence of Mercury, *Phys. Rev. Lett.* **94**, 034501 (2005).
- [25] D. Funfschilling and G. Ahlers, Plume Motion and Large-Scale Circulation in a Cylindrical Rayleigh-Bénard Cell, *Phys. Rev. Lett.* **92**, 194502 (2004).
- [26] H.-D. Xi, S.-Q. Zhou, Q. Zhou, T.-S. Chan, and K.-Q. Xia, Origin of the Temperature Oscillation in Turbulent Thermal Convection, *Phys. Rev. Lett.* **102**, 044503 (2009).
- [27] Q. Zhou, H.-D. Xi, S.-Q. Zhou, C. Sun, and K.-Q. Xia, Oscillations of the large-scale circulation in turbulent Rayleigh-Bénard convection: The sloshing mode and its relationship with the torsional mode, *J. Fluid Mech.* **630**, 367 (2009).

- [28] E. Brown and G. Ahlers, The origin of oscillations of the large-scale circulation of turbulent Rayleigh-Bénard convection, *J. Fluid Mech.* **638**, 383 (2009).
- [29] T. Vogt, S. Horn, A. M. Grannan, and J. M. Aurnou, Jump rope vortex in liquid metal convection, *Proc. Natl. Acad. Sci. USA* **115**, 12674 (2018).
- [30] E. Brown and G. Ahlers, Effect of the Earth's Coriolis force on turbulent Rayleigh-Bénard convection in the laboratory, *Phys. Fluids* **18**, 125108 (2006).
- [31] J.-Q. Zhong, H.-M. Li, and X.-Y. Wang, Enhanced azimuthal rotation of the large-scale flow through stochastic cessations in turbulent rotating convection with large Rossby numbers, *Phys. Rev. Fluids* **2**, 044602 (2017).
- [32] S. Sterl, H.-M. Li, and J.-Q. Zhong, Dynamical and statistical phenomena of circulation and heat transfer in periodically forced rotating turbulent Rayleigh-Bénard convection, *Phys. Rev. Fluids* **1**, 084401 (2016).
- [33] K. R. Sreenivasan, A. Bershadskii, and J. J. Niemela, Mean wind and its reversals in thermal convection, *Phys. Rev. E* **65**, 056306 (2002).
- [34] R. Benzi, Flow Reversal in a Simple Dynamical Model of Turbulence, *Phys. Rev. Lett.* **95**, 024502 (2005).
- [35] F. F. Araujo, S. Grossmann, and D. Lohse, Wind Reversals in Turbulent Rayleigh-Bénard Convection, *Phys. Rev. Lett.* **95**, 084502 (2005).
- [36] C. Resagk, R. du Puits, A. Thess, F. V. Dolzhansky, S. Grossmann, F. F. Araujo, and D. Lohse, Oscillations of the large scale wind in turbulent thermal convection, *Phys. Fluids* **18**, 095105 (2006).
- [37] E. Brown and G. Ahlers, A model of diffusion in a potential well for the dynamics of the large-scale circulation in turbulent Rayleigh-Bénard convection, *Phys. Fluids* **20**, 075101 (2008).
- [38] M. Chandra and M. K. Verma, Dynamics and symmetries of flow reversals in turbulent convection, *Phys. Rev. E* **83**, 067303 (2011).
- [39] B. Podvin and A. Sergent, A large-scale investigation of wind reversal in a square Rayleigh-Bénard cell, *J. Fluid Mech.* **766**, 172 (2015).
- [40] D. Giannakis, A. Kolchinskaya, D. Krasnov, and J. Schumacher, Koopman analysis of the long-term evolution in a turbulent convection cell, *J. Fluid Mech.* **847**, 735 (2018).
- [41] A. Vasiliev, P. Frick, A. Kumar, R. Stepanov, A. Sukhanovskii, and M. K. Verma, Transient flows and reorientations of large-scale convection in a cubic cell, *Intl. Commun. Heat Mass Transfer* **108**, 104319 (2019).
- [42] E. Brown and G. Ahlers, Azimuthal asymmetries of the large-scale circulation in turbulent Rayleigh-Bénard convection, *Phys. Fluids* **20**, 105105 (2008).
- [43] M. Assaf, L. Angheluta, and N. Goldenfeld, Rare Fluctuations and Large-Scale Circulation Cessations in Turbulent Convection, *Phys. Rev. Lett.* **107**, 044502 (2011).
- [44] H. Song, E. Brown, R. Hawkins, and P. Tong, Dynamics of large-scale circulation of turbulent thermal convection in a horizontal cylinder, *J. Fluid Mech.* **740**, 136 (2014).
- [45] Y. Liu and R. E. Ecke, Heat transport measurements in turbulent rotating Rayleigh-Bénard convection, *Phys. Rev. E* **80**, 036314 (2009).
- [46] K. Bai, D. Ji, and E. Brown, Ability of a low-dimensional model to predict geometry-dependent dynamics of large-scale coherent structures in turbulence, *Phys. Rev. E* **93**, 023117 (2016).
- [47] N. Foroozani, J. J. Niemela, V. Armenio, and K. R. Sreenivasan, Reorientations of the large-scale flow in turbulent convection in a cube, *Phys. Rev. E* **95**, 033107 (2017).
- [48] A. Vasiliev, A. Sukhanovskii, P. Frick, A. Budnikov, V. Fomichev, M. Bolshukhin, and R. Romanov, High Rayleigh number convection in a cubic cell with adiabatic sidewalls, *Intl. J. Heat Mass Transfer* **102**, 201 (2016).
- [49] V. D. Zimin and A. I. Ketov, Turbulent convection in a cubic cavity heated from below, *Fluid Dyn.* **13**, 594 (1978).
- [50] G. Zocchi, E. Moses, and A. Libchaber, Coherent structures in turbulent convection: An experimental study, *Physica A* **166**, 387 (1990).
- [51] X. L. Qiu and K.-Q. Xia, Viscous boundary layers at the sidewall of a convection cell, *Phys. Rev. E* **58**, 486 (1998).
- [52] L. Valencia, J. Pallares, I. Cuesta, and F. X. Grau, Turbulent Rayleigh-Bénard convection of water in cubical cavities: A numerical and experimental study, *Intl. J. Heat Mass Transfer* **50**, 3203 (2007).

- [53] D. Funfschilling, E. Brown, and G. Ahlers, Torsional oscillations of the large-scale circulation in turbulent Rayleigh-Bénard convection, *J. Fluid. Mech.* **607**, 119 (2008).
- [54] E. Brown, A. Nikolaenko, and G. Ahlers, Reorientation of the Large-Scale Circulation in Turbulent Rayleigh-Bénard Convection, *Phys. Rev. Lett* **95**, 084503 (2005).
- [55] E. Brown, D. Funfschilling, A. Nikolaenko, and G. Ahlers, Heat transport by turbulent Rayleigh-Bénard convection: Effect of finite top- and bottom-plate conductivities, *Phys. Fluids* **17**, 075108 (2005).
- [56] D. Ji and E. Brown, Oscillation in the temperature profile of the large-scale circulation of turbulent convection induced by a cubic container, [arXiv:2003.00067](https://arxiv.org/abs/2003.00067).
- [57] H. A. Kramers, Brownian motion in a field of force and the diffusion model of chemical reactions, *Physica* **7**, 284 (1940).
- [58] E. Villermaux, Memory-Induced Low Frequency Oscillations in Closed Convection Boxes, *Phys. Rev. Lett.* **75**, 4618 (1995).
- [59] E. Brown, D. Funfschilling, and G. Ahlers, Anomalous Reynolds-number scaling in turbulent Rayleigh-Bénard convection, *J. Stat. Mech.* (2007) P10005.